Conf-920804--1

LA-UR-91- 4095

[illegible]

Los Alamos National Laboratory is operated by the University of California for the United States Department of Energy under contract W-7405 ENG-36

TITLE: A PHENOMENOLOGICAL MODEL OF THE THERMAL-HYDRAULICS OF CONVECTIVE BOILING DURING THE QUENCHING OF HOT ROD BUNDLES PART II: ASSESSMENT OF THE MODEL WITH STEADY-STATE AND TRANSIENT POST-CHF DATA

LA-UR--91-4095

DE92 005051

AUTHOR(S): Cetin Unal
Ralph Nelson

SUBMITTED TO: The 28th ASME/AIChe/ANS National Heat Transfer Conference;
San Diego, California; August 9-12, 1992

DISCLAIMER

This report was prepared as an account of work sponsored by an agency of the United States Government. Neither the United States Government nor any agency thereof, nor any of their employees, makes any warranty, express or implied, or assumes any legal liability or responsibility for the accuracy, completeness, or usefulness of any information, apparatus, product, or process disclosed, or represents that its use would not infringe privately owned rights. Reference herein to any specific commercial product, process, or service by trade name, trademark, manufacturer, or otherwise does not necessarily constitute or imply its endorsement, recommendation, or favoring by the United States Government or any agency thereof. The views and opinions of authors expressed herein do not necessarily state or reflect those of the United States Government or any agency thereof.

By acceptance of this article, the publisher recognizes that the U. S. government retains a nonexclusive, royalty-free license to publish or reproduce the published form of this contribution, or to allow others to do so, for U. S. Government purposes.

The Los Alamos National Laboratory requests that the publisher identify this article as work performed under the auspices of the U. S. Department of Energy.

Los Alamos

Los Alamos National Laboratory
Los Alamos, New Mexico 87545

MASTER

A PHENOMENOLOGICAL MODEL OF THE THERMAL-HYDRAULICS OF CONVECTIVE BOILING DURING THE QUENCHING OF HOT ROD BUNDLES
PART II: ASSESSMENT OF THE MODEL WITH STEADY-STATE AND TRANSIENT POST-CHF DATA

by

Cetin Unal and Ralph Nelson

Los Alamos National Laboratory
Nuclear Technology and Engineering Division
Engineering and Safety Analysis Group
Los Alamos, NM 87545

ABSTRACT

After completing the thermal-hydraulic model developed in a companion paper, we performed assessment calculations of the model using steady-state and transient post-critical heat flux (CHF) data. This paper discusses the results of those calculations.

The hot-patch model, in conjunction with the other thermal-hydraulic models, was capable of modeling the Winfrith post-CHF hot-patch experiments. The hot-patch model kept the wall temperatures at the specified levels in the hot-patch regions and did not allow any quench-front propagation from either the bottom or the top of the test section. Among the four Winfrith runs selected to assess the hot-patch model, the average deviation in hot-patch power predictions was 15.4%, indicating reasonable predictions of the amount of energy transferred to the fluid by the hot patch.

The interfacial heat-transfer model tended to slightly underpredict the vapor temperatures. The maximum difference between calculated and measured vapor superheats was 20%, with a 10% difference for the remainder of the runs considered. The wall-to-fluid heat transfer was predicted reasonably well, and the predicted wall superheats were in reasonable agreement with measured data with a maximum relative error of less than 13%. The effects of pressure, test section power, and flow rate on the axial variation of tube wall temperature are predicted reasonably well for a large range of operating parameters. A comparison of the predicted and measured local wall superheats at the beginning, middle, and end of the test tube for 20 post-CHF tests indicated that the maximum average deviation was 15.2%. The vapor superheat is under-predicted, and the average deviation was found to be 37.6%.

The thermal-hydraulic model in TRAC/PF1-MOD2 was used to predict the axial variation of void fraction as measured in Winfrith post-CHF tests. The predictions for reflood calculations were reasonable. The relative error was 40% at locations just downstream of the post-agitated inverted annular flow and 10% at locations far downstream of the post-agitated inverted annular flow. The model correctly predicted the trends in void fraction as a result of the effect of pressure and power, with the effect of pressure being more apparent than that of power.

The predicted precursory cooling rates in Berkeley transient reflood tests were in reasonably good agreement with the measured data. The predicted quench-front velocities (the rewetting velocity) and their variation along the test tube also were found to be in reasonably good agreement with the measured data. The comparison of the average predicted and measured rewetting velocities between five thermocouple locations in eight Berkeley tests showed 26% average and 40% standard deviation. For high wall heat fluxes, oscillations associated with the void fraction prediction existed in the predictions.

I. INTRODUCTION

As pointed out in a companion paper (1), a significant number of experimental and analytical studies reporting on post-critical heat flux (CHF) boiling and quenching have been published in the last two decades. However, a large amount of scatter still exists between the predictions from published correlations and measured data (2). This disagreement between the models and data was attributed to the fact that the hydraulic and heat-transfer models typically are developed independent of one another and, when combined, produce a large part of the scatter. Thus, even when "the best heat transfer and hydraulic models" are combined and compared with either the original data sets or new ones, significant scatter is not surprising. To develop more accurate models, information on heat transfer must be integrated with the best available hydrodynamic data in the model development process. Ultimately, an experiment that measures all the required quantities is needed;

however, the state of the art in measurements is not capable yet of doing such an experiment.

The problem of "integrated model development" is compounded in two-phase, two-fluid, thermal-hydraulic computer codes, such as TRAC, that solve the mass, momentum, and energy equations for each phase. To accomplish this solution, they require closure relationships to determine mass, momentum, and heat-transfer interchange between the phases and between both heated or unheated structures and the phases. Because phasic closure relationships are generally not available, code developers are forced to infer these phasic relationships based on limited information available from the data they are analyzing. This frequently is done by modifying existing models and combining these modified models to represent the different phenomena for the required phasic contributions. This process has received much debate.

During the development of the reflood model, our approach to defining these phasic closure relationships was to use correlations known to apply to a given regime for a particular closure quantity wherever possible. However, the original correlation frequently could not be applied directly but had to be modified. For those cases, we tried to use the "kernel or functional dependence" of the original correlation and modify only its magnitude by use of a multiplier. This assumes the original model developer was able to capture and represent the functional dependence of the controlling physical quantities. When no correlations were available for given regimes, we tried to define known bounding regimes and use a weighting function between the known regimes to represent the unknown quantities. This assumes the process is continuous and bounded between the two known regimes. In two instances for wall heat transfer, we had to develop separate models to represent the phenomena—the models for transition boiling and the near-wall-liquid post-CHF film boiling effect. The overall model, which is discussed in the companion paper (1), was implemented into the TRAC-PF1/MOD2 computer code.

This paper will not discuss the adjustment process of the modifying constants and weighting factors (empirical constants). The details of this process are available in Ref. (6), and a brief discussion of this process is presented in Sec. II. We will discuss the results obtained when the model is used to predict steady-state and transient post-CHF experimental results to provide an independent assessment. Independent assessment of the final model, with 21 Winfrith post-CHF tests (4,10) having different operating conditions, is presented in Sec. III. A The calculated and measured wall and vapor temperatures and void fraction were compared for the steady-state data base.

The assessment of the thermal-hydraulic model with transient quenching data was performed using a series of eight Berkeley reflood tests (11). These tests were selected in such a way that the effect of mass flux, power, and inlet fluid temperature on the reflood behavior could be investigated to identify areas for possible further improvements. The basic parameters compared were the rate of variation in wall temperatures (indicating the degree of the precursory cooling rate), the quench times of thermocouple locations, and the quench-front velocity (rewetting velocity) between the thermocouple locations. The results of this assessment work for transient data are discussed in Sec. III.B.

II. SUMMARY OF THE PROCEDURE USED TO ADJUST THE EMPIRICAL CONSTANTS IN THE MODEL

The adjustment of the empirical constants involved several iterations. Briefly, the empirical constants for the interfacial drag model were found using a reasonable set of coefficients for the wall heat transfer and CCTF Run 14 (3). Then, fine adjustment and correlation of the near-wall-liquid post-CHF film boiling effect were done for the wall and interfacial heat transfer using a set of six Winfrith steady-state post-CHF hot-patch runs (4). After implementation of the adjusted and correlated heat-transfer coefficients, the interfacial drag model again was checked and readjusted as needed with the CCTF Run 14 pressure drop data. The last step involved evaluating the B-coefficient used in the transition boiling model (see Ref. 1). The B-coefficient was determined in such a way that the predicted and measured quench-front propagation rates were reasonable in CCTF Run 14 and Lehigh rod bundle (5) tests.

The adjustment of the empirical constants used in the interfacial drag models could best be done using steady-state experimental data obtained for each individual regime. However, such data are not yet available in the literature for the inverted annular flow (IAF) regimes. The data we used in the development of the drag model is the transient quasi-steady pressure drop data obtained for CCTF Run 14. During a reflood test, any particular elevation in the test section experiences dispersed, agitate, rough-wavy IAF, smooth IAF, transition boiling, and finally nucleate boiling. Although the presence of these regimes is not measured directly, the amount of liquid that occurs between any two elevations is indicated by the pressure drop between them. Thus, between any two particular elevations (the distance between the pressure taps) where a known flow regime exists over a given time window, the pressure drop data can be used to determine the necessary empirical constants.

We adjusted the empirical constants described in interfacial drag models [see Ref. (6)] by reasonably matching the pressure drop data in this time-window-by-window method. The problem that makes this adjustment somewhat complicated is that the pressure taps are spaced far enough apart (about 0.6 m) that multiple regimes occur between them. The only regimes that occur uniquely between the ports are nucleate boiling, dispersed flow, and perhaps the post-agitated regime. Thus, one cannot determine the necessary empirical constants uniquely for smooth IAF, rough-wavy IAF, and agitated IAF. We can see only the spatial integrated effect, which typically includes these regimes plus one of the other regimes.

This drag adjustment process is cumbersome because of the hydraulic feedback that occurs between the drag flow regimes. Fortunately, although the heat transfer and drag are coupled, they are not tightly coupled, which allows for separate adjustment steps. This drag feedback effect can be minimized by working the problem from bottom up, i.e., nucleate boiling through film boiling. Although the technique yields reasonable results, as noted above, it is not possible to match pressure drop data in all of the flow regimes simultaneously.

To adjust the empirical constants associated with the wall and interfacial heat-transfer models, a limited set of Winfrith steady-state post-CHF hot-patch tests listed below was used. The weighting factors and constants for the wall-to-fluid and interfacial heat transfer were adjusted by predicting the measured wall and vapor temperatures for six selected Winfrith post-CHF tests (Runs 149, 177, 122, 104, 98, 157). The mass flux was varied, and the heat flux, pressure, and inlet subcooling were kept constant for Runs 149, 177, 122, 104, and 98. For each of these five tests, a fixed empirical coefficient used in the near-wall liquid model was determined by matching experimental wall and vapor temperature profiles with the calculated values as close as possible. Next, these coefficients were correlated in terms of the vapor Reynolds number defined at the beginning of the agitated IAF for each of the runs.

Run 157 was used to determine the effect of pressure on the correlated near-wall wall-to-liquid heat transfer. To predict the measured wall and vapor temperatures in this high-pressure run, the vapor Reynolds number dependent constant required a decrease. Therefore, we introduced an exponent to the vapor Reynolds number.

In the absence of steady-state data without the influence of hot patches, it is difficult to determine the B-coefficient required by the transition boiling model (see Ref. 1) and that controls the rate of the quench-front propagation. The B-coefficient was adjusted by matching the experimental quench-front velocity of CCTF Run 14 and the Lehigh rod bundle test. The Capillary and vapor Reynolds numbers at the CHF point, which control the selection of the B-coefficient, vary significantly during these transient calculations. The initial results in predicting the quench-front propagation in CCTF Run 14 and Lehigh tests indicated that two different proportionality constants were needed to match the experimental data. The CCTF Run 14 test included flow conditions with relatively high vapor Reynolds number (time-average value), indicating the vapor flow was mostly turbulent. The time-averaged Reynolds number in the Lehigh test was less than 2000, indicating the vapor flow was laminar during the transient. Thus, the B-coefficient was assumed to be 16 for a vapor Reynolds number less than 2000 and 10 for a vapor Reynolds number higher than 2000.

III. DISCUSSION OF RESULTS AND COMPARISONS

The description of the each test selected for this assessment work, the experimental test procedure, and the TRAC input models are not discussed in this paper. They are available in Ref. (6). The results and lessons learned from the assessment of the final model with transient (Berkeley reflood) and steady-state (Winfrith steady-state) data are discussed below. All calculations discussed in this paper were performed in a transient mode. A "snapshot" of the transient calculation when thermal-hydraulic conditions had stabilized was analyzed and compared with the steady-state data.

A. Assessment of the Model with Winfrith Steady-State Post-CHF Data

This section discusses the assessment of the post-CHF film boiling model using Winfrith steady-state hot-patch experiments. The range of parameters of the Winfrith runs used in this work is listed below. There are two sets of data; the Series 100 and 200 tests include wall and vapor superheat data, the Series 400 and 500 data includes wall and vapor superheat as well as void fraction data. Section III.A.1

TABLE I

WINFRITH STEADY-STATE POST-CHF RUNS USED FOR THE ASSESSMENT OF THE MODEL

Run No.	G (kg/m^2s)	q (W/cm^2)	P (bar)	Tin (°C)
448	100	1.68	5.0	5.0
451	100	1.1	5.0	5.0
446	100	2.54	5.0	5.0
434	100	1.68	2.0	5.0
456	100	1.68	10.1	5.0
441	50	1.68	5.0	5.0
366	201	1.68	5.0	5.0
364	202	2.8	5.0	5.0
379	505	2.8	5.0	5.0
412	2004	2.8	5.0	5.0
176	102	1.713	2.0	4.7
179	103	0.747	2.01	5.2
136	49	2.229	5.0	7.3
135	48	1.434	10.0	6.2
150	48	1.449	2.02	4.9
157	102	2.849	10.0	2.4
194	199	2.252	5.0	4.5
76	217	4.551	9.9	6.5
95	1010	3.552	2.1	6.2
193	104	2.8	4.99	26.4
161	102	2.818	4.93	4.0

discusses the results obtained from hot patch model, and Sec. III.A.2 presents the final results and comparison.

1. Assessment of the Hot-Patch Model with Winfrith Steady-State Post-CHF Data. One major difficulty in conducting steady-state post-CHF experiments is preventing propagation of the quench front into the test section. Using the hot-patch technique (6) allows researchers to create stabilized post-CHF conditions throughout the test section. A hot-patch model was developed as a feature of the slab heat structure component in TRAC computer program (6). The axial elevations of the hot-patch inlet and outlet and hot-patch temperatures are input parameters to this model. The hot-patch model uses a very high convective-heat-transfer coefficient on the outer surface of the slab to simulate an imaginary heat source at the specified hot-patch temperature. Thus, the necessary energy to prevent the quench-front propagation could be provided by this heat source. The boundary conditions at the inner surface of the slab in the test section are determined by the convective post-CHF conditions. This assessment work modeled both the lower and upper hot patches used in Winfrith steady-state post-CHF tests.

The calculated wall surface temperature histories at eight different axial elevations are shown in Fig. 1 for Run 176 to illustrate that the transient solution had converged. The locations of the inlet and outlet of the lower and upper hot patches are 0.16, 0.2, 1.12, and 1.256 m, respectively. The wall surface temperatures do not change after 100 s, indicating a converged solution and that steady-state post-CHF conditions were obtained at each elevation. The quench front is located 2.6 mm upstream of the lower hot patch. The wall temperature for the inside of the tube at the beginning of the lower hot patch is 746 K, less than the specified hot-patch temperature of 875 K. However, 1 cm downstream of the hot-patch inlet, the calculated hot-patch surface temperature is calculated to be 864 K, indicating that the quench front is held at the beginning of the lower hot patch. The wall temperatures at the beginning and end of the upper hot patch do not change with time and are at higher temperatures (875 K), indicating there is no quench-front propagation from the top of the test section.

Other runs showed similar characteristics for convergence to steady-state conditions. Therefore, snapshot results of calculations at a time of 250 s were used for the steady-state data-model comparison unless otherwise mentioned. In addition, the relative error between predicted and calculated parameters is defined as the absolute value of the ratio of the difference between measured and calculated parameters to the measured parameter.

The hot-patch power is not an input parameter to the TRAC model. The hot patch is modeled by a special heat-structure component with its temperature specified as discussed in companion papers (1,2). The amount of energy supplied by the hot patch is important in determining the thermal-hydraulic conditions downstream of the hot-patch location. The calculated and measured hot patch power for Runs 176, 446, 451, 448, and 434 are shown in Fig. 2; the average deviation was found to be 15.4%. This type of imbalance in total energy transferred to the fluid will not change the hydraulic conditions at the test section inlet significantly. For example, for Run 451, the equilibrium quality at the exit of the hot patch (no conduction downstream of the hot patch is considered) is 1.7% if the calculated hot-patch power is used and 2.3% if the measured hot-patch power is used. A small change in inlet quality is not expected to significantly change the thermal response of the wall. Therefore, the hot-patch power predicted by the model is reasonable and is expected to be so for other ranges of parameters.

2. Assessment of the Final Model with the Winfrith Steady-State Post-CHF Data. We will first discuss the prediction of void fraction for Winfrith steady-state post-CHF data. The wall and vapor temperature predictions will be presented for the same data base.

Void fractions at three axial elevations (0.13, 0.445, and 0.795 m from the hot-patch outlet) were calculated from the fluid density measurements obtained using a gamma densitometer. The overall accuracy of the void fraction measurements was reported as ±3% (11). The void fraction data for the runs 434, 448, 456, 451, and 446 (listed in Table I) were plotted against the equilibrium quality in Figs. 10 and 12 of Ref. 11. For each run, there were three void fraction measurements corresponding to the three densitometer positions. The measured void fractions used in this paper for comparison purposes were taken from Figs. 10 and 12 of Ref. 10 for Runs 434, 448, 456, 451, and 446.

We first discuss the results obtained for Run 434, which was performed at 2 bar and 100 kg/m^{2}s, because the hydraulic model in Ref. 1 was developed using Cylindrical Core Test Facility (CCTF) pressure-drop data (13) obtained at 2 bar.

Figure 3 shows the predicted and measured void fractions for Run 434. The calculated interfacial drag coefficient, an important parameter in determining the void fraction, also is plotted in the figure. Swinnerton et al. (10) reported the uncertainty in the void fraction measurements to be 3% of the measured values. The experimental uncertainty for each measured void fraction data point is indicated by uncertainty bars in the figure. The calculated locations of IAF regimes for this run are listed in Table II.

No highly dispersed flow regime is predicted to occur in this run. That regime is assumed to occur when the void fraction at a particular location is higher than 98%. The void fraction at the end of the test section was calculated to be 0.958, indicating that no highly dispersed flow occurred. The predicted void fraction at the elevation of 0.995 m (from the hot-patch inlet) agreed with the measured data very well, as indicated in Fig. 3.

The elevation 0.995 m is located at the upper end of the predicted post-agitated IAF region. At the elevation of 0.645 m, the predicted void fraction showed 8.6% relative error. As the axial distance decreased (Z = 0.33 m is just downstream of

TABLE II
CALCULATED LOCATIONS OF INVERTED ANNULAR FLOW REGIMES

Inverted Annular Flow Regime	Location
CHF	0.1614 m
Transition Boiling Region	0.1614 m < Z < 0.1629 m
Smooth IAF Regime	0.1629 m < Z < 0.1654 m
Rough-Wavy IAF Regime	0.1654 m < Z < 0.2276 m
Agitated IAF Regime	0.2276 m < Z < 0.2490 m
Post-Agitated IAF Regime	0.2490 m < Z < 1.1174 m

agitated IAF), the relative error between measured and predicted values increased to 30%.

Table III lists the calculated and measured void fractions for Run 434 and others.

The amount of vapor generation and the interfacial drag coefficient are among the most important parameters in determining the cell void fraction. The vapor generation rate is controlled by the wall-to-liquid heat transfer and the interfacial heat transfer. As will be shown and discussed later, the prediction of wall temperature is reasonable, and most of the vapor temperatures were under-predicted, which indicates an over-prediction of interfacial heat transfer. Thus,

TABLE III
CALCULATED AND MEASURED VOID FRACTIONS

	Calculated			Measured		
Z	0.33 m	0.645 m	0.995 m	0.33 m	0.645 m	0.995 m
Run No						
448	0.522	0.795	0.896	0.783	0.904	0.961
456	0.399	0.698	0.866	0.669	0.849	0.933
434	0.61	0.864	0.941	0.873	0.945	0.976
451	0.452	0.716	0.821	0.753	0.867	0.916
446	0.628	0.865	0.945	0.831	0.938	0.976

the under-prediction of the void fraction just downstream of the agitated IAF is most probably a result of under-prediction of the interfacial drag coefficients in the post-agitated region.

In this post-agitated region, the present formulation applies a void-fraction-dependent weighting between the interfacial drag coefficients (IFDCs) obtained for the agitated and highly dispersed IAF IFDC models (see Ref. 1). However, we did not formulate an IFDC model for the agitated IAF region because of its complex hydrodynamic structure and the lack of experimental data for this region. Instead, we used the model developed for rough-wavy IAF with a multiplication factor. This was done on the following basis. It is expected that the IFDC should increase gradually when the flow regime changes from smooth to rough-wavy IAF. In agitated IAF, because of the increase in the interfacial surface area, the IFDC is expected to be higher than that of rough-wavy IAF. Thus, the IFDC in the agitated IAF region is calculated by multiplying $C_{i,rw}$ by a factor of 1.25 (the empirical constant), and the IFDC for post-agitated IAF is given by

$$C_{i,pa} = 1.25\, C_{i,rw} + (C_{i,df} - 1.25\, C_{i,rw}) \left[\frac{\alpha - \alpha_{ag}}{\alpha_{df} - \alpha_{ag}} \right]^{0.5} . \qquad (1)$$

Because the measured and calculated values near the exit of the test section (where the drag coefficient $\approx C_{i,df}$) show reasonable agreement, the under-prediction of the void fraction just downstream of the agitated IAF may be a result of the rough-wavy multiplier (1.25) being too low. However, it should be remembered that no data were available to us at the time of model development. With this in mind, it can be concluded that, although the void fraction is under-predicted just downstream of the agitated IAF, the prediction showed good agreement at the higher elevations.

The effect of system pressure on void fraction is shown in Fig. 4 and Table III. Figure 4 shows the predicted and measured void fractions for Runs 434, 448, and 456. These runs were performed at the same mass flux, power, and inlet subcooling but at different pressures (varying from 2 to 10 bar). The locations of the IAF regimes do not change significantly in these runs and are similar to those given for Run 434. The measured values indicate that the void fraction at a given elevation decreases with increasing pressure. The decrease in void fraction is extreme at lower elevations (just downstream of the agitated flow). This trend is predicted by the model. However, the calculated decrease in void fraction with increasing pressure is relatively greater than that observed in the measured data. Consequently, the relative error between the measured and predicted void fraction at a given elevation is also greater. The relative errors for axial elevations of 0.33, 0.645 and 0.995 m at 10 bar (Run 456) are 40%, 18%, and 7.2%, respectively.

Figure 5 shows the predicted and measured void fraction profiles for Run 446, which was performed with the same mass flux, pressure, and inlet subcooling as Run 448 but with a higher power. When the test section net power is increased to 2.54 kW (8.03 W/cm^2), the calculated axial IFDC profile is shifted slightly upward, but the shift in the axial void fraction profile is not significant (see Figs. 4 and 5). The effect of the power is more clearly illustrated in Fig. 6. In this figure, we plot the predicted and measured void fractions for Runs 451, 448, and 446. In these runs, the mass flux, pressure, and inlet subcooling are the same, but the test section power was changed.

The experimentally observed parametric trend in the measured void fractions with test section power is predicted reasonably well; the void fraction decreases slightly with decreasing test section power with similar void fraction magnitudes at each of the axial elevations. At the lowest test section power (Run 451), the relative errors at elevations of 0.33, 0.645, and 0.995 m are 40%, 17.5%, and 10.3%, respectively.

From the above comparisons, it can be concluded that the thermal-hydraulic model developed in a companion paper (1) predicts the measured void fraction with a 10% error (keep in mind that there is a 3% uncertainty in the measurements) at locations far downstream of the post-agitated IAF for the pressure range of 2–10 bar and the heat flux range of 3.6–8.03 W/cm^2. The predictions deviate from the measured values by about 40% just downstream of the post-agitated IAF. This axial distribution of error is systematic for all the runs studied. The predictions become more accurate for lower pressures and higher heat fluxes. The effect of pressure is more apparent than the effect of heat flux.

The typical calculated and measured wall and vapor temperatures are shown in Fig. 7 for Runs 176 and 179 as a function of height. The locations of the flow regimes and hot patches also are indicated in the figure. The quench front (indicated as the CHF point) is located just 2.6 mm upstream of the lower hot patch. The first half of the lower hot patch experiences smooth IAF, whereas the other half is in rough-wavy IAF. The calculated phasic heat fluxes [wall-to-liquid (Denham and near-wall contributions), and wall-to-vapor (Webb-Chen)] are presented in Fig. 8. In smooth IAF, the wall-to-liquid heat flux is relatively high and decreases sharply with increasing height. The heat transfer is governed by the wall-to-liquid contribution, and no wall-to-vapor contribution is assumed in this regime. The calculated wall temperatures suggest that the wall-to-liquid heat transfer is predicted reasonably well.

The trend of wall temperature in the second half of the hot patch (where rough-wavy IAF starts) changes. The wall temperature decreases to 830 K at the end of rough-wavy IAF, which is located 0.2143 m from the test section inlet. The calculated and measured wall temperatures imply that the wall-to-liquid heat transfer is predicted well in rough-wavy IAF. The near-wall liquid contribution gradually increases with increasing height. The wall-to-liquid heat-transfer contribution by the Denham correlation gradually decreases but is still mainly responsible for transferring the energy from the wall in rough-wavy IAF.

A comment concerning the prediction of the wall temperatures for the steady-state Winfrith runs is appropriate at this point. As the reader will observe in the comparisons of numerous Winfrith runs, the prediction of the wall temperatures just downstream of the exit of the lower hot patch is quite difficult. This difficulty arises from the very complex interactions associated with axial conduction between the heater tube and the lower hot patch, the short axial distances over which most of the IAF regimes occur, and their occurrence at or near the exit of the hot patch. These difficulties typically result in either an over- or under-prediction of the temperature just downstream of the lower hot patch exit. Errors in this exit behavior prediction frequently produces a "rigid body" offset in the wall temperatures which are followed by more gradual post-CHF behavior. Thus, it is possible to miss the prediction in the drop/rise of wall temperature exiting the lower hot patch yet predict the remaining post-CHF behavior quite wall. Run 179 in Fig. 7 is an example of such a prediction. The predicted wall temperature parallels the data indicating the wall heat transfer coefficient was the same for the two cases. We currently view the prediction of the correct slope downstream of the lower hot patch exit behavior as being more important than the prediction of that exit behavior itself.

The predicted wall temperature in agitated IAF decreases further and is overpredicted by about 10°C at the end of the agitated region. In this region, no void fraction weighting is applied to the near-wall wall-to-liquid heat-transfer coefficient. Therefore, the wall-to-liquid heat flux does not vary significantly, as shown in Fig. 8. It decreases very slowly with increasing axial location until the void fraction becomes about 45%. After this location, it gradually decreases because of the applied void-dependent weighting. The wall-to-vapor heat flux increases with increasing height but its rate of increase is less than the decrease of wall-to-liquid heat flux.

The wall temperature at the beginning of the post-agitated IAF increases with increasing axial distance. The calculated wall temperatures between 0.23–0.45 m are about 10°C higher than measured values. After 0.5 m, the agreement between calculated and measured wall temperatures becomes very good. The slope of the wall temperature profile agrees with experimental data, indicating that the overall wall-to-fluid heat transfer is predicted very well in this region. The near-wall wall-to-liquid heat flux decreases with increasing height, as shown in Fig. 8. At 50 cm, it is about 40% of the wall-to-vapor heat flux, whereas it becomes approximately 6% of the wall-to-vapor heat flux at the end of the test section. The interfacial heat-transfer model uses a relatively high heat-transfer coefficient for the heat transfer from the interface to the vapor in smooth, rough-wavy, and agitated IAFs. Therefore, the calculated vapor temperatures are close to the saturation temperature of the fluid. In post-agitated IAF, the interface-to-vapor HTC drops to very low values. It has been observed experimentally that the evaporation process in dispersed flow is inefficient relative to that just downstream of the CHF point (8). The axial vapor temperature profile measured was S-shaped, low or close to the saturation temperature in the region near to the CHF point, and high in the dispersed flow region (far-region of the CHF point) (9). Using a weighted interface-to-vapor heat-transfer coefficient allows the vapor temperature to be superheated gradually in post-agitated IAF, as shown in Fig. 7. The predicted vapor temperature increases gradually and becomes 649 K in the 16th cell, whereas the measured vapor temperature was 738 K, indicating an 89°C under-prediction (a 12% relative error). It can be concluded that the overall predictions of the interfacial and wall-to-fluid heat transfer for Run 176 agree with the experimental data reasonably well.

Figure 7 also shows the calculated and measured axial wall and vapor temperature profiles for Run 179. Run 179 has a 45% lower heat flux than Run 176 while retaining the same mass flux and pressure. The locations of the IAFs are similar to those observed in Run 176. This is because Ishii's flow-regime criteria consider the capillary number defined at the CHF point, which is similar in Runs 176 and 179. The predicted heat transfer in smooth and rough-wavy IAFs showed good agreement with the measured data. However, the agitated and post-agitated IAFs heat fluxes were slightly over-predicted. Therefore, the wall temperatures are under-predicted by about 60°C at 0.3 m. However, the predicted and measured wall temperature profiles in post-agitated IAF agreed with each other very well. The predicted vapor temperature is approximately 100°C lower than the measured value. This also causes the wall temperature to be shifted slightly to lower values. The under-prediction of the wall temperature indicates a relative superheat error of 8%.

Although we made a parametric study for the effect of operating parameters on the wall and vapor temperatures for the Series 100 set of data (available in Ref. 6), because of page limitations, we will discuss only the parametric variation of the wall temperature for runs in the Series 400. The results obtained from the one-hundred and four-hundred series were similar.

Figure 9 shows the effect of pressure on predicted and measured axial wall temperature profiles for Runs 434, 448, and 456. The locations of the flow regimes do not change significantly because the mass flux is the same for all runs shown in the figure. The region downstream of the hot patch experiences mostly post-agitated IAF. The wall temperature just downstream of the hot-patch region for all runs is under-predicted, and the under-prediction is greater at higher pressures. The predicted decrease in wall temperatures levels off at the end of agitated IAF, and the wall temperatures begin to increase at a rate similar to that seen in the measured data. The wall temperature is over-predicted by about 50°C at the lowest pressure (2 bar) and is under-predicted by about 50°C at the higher pressures (5 and 10 bar). However, the model correctly predicts the trend in measured wall temperature with changing pressure; the wall temperatures decrease with increasing pressure. As will be shown later, the under- and over-predictions of wall temperature show low relative errors. It is important to note that the slopes of the predicted wall temperature profiles, especially between flow-regime transitions, agree with the measured data reasonably well.

Figure 10 shows the effect of test section power on the predicted and measured axial wall temperature profiles. At the lowest test power, 1.1 kW in Run 451, the predicted wall temperatures are under-predicted up to an axial elevation of 0.3 m. The under-prediction decreases in the post-agitated region, and the wall temperatures agree with the measured data. However, at the end of tube, the rate of increase in wall temperature is under-predicted so that the resulting wall temperatures are less than measured values by 50°C. The axial wall temperature profiles are predicted reasonably well. The measured wall temperatures increase with increasing test section power, and this trend is reflected in the predictions as well. The wall temperatures in the hot-patch region, where the smooth, rough-wavy, and part of the agitated IAF exist, are under-predicted. In the previous paragraphs, we showed that an increase in pressure causes the wall temperatures to be under-predicted. Because the runs in Fig. 10 were performed at the higher pressure of 5 bar, the under-prediction of wall temperatures in Fig. 10 could be a result of the combined effect of pressure and power. However, the effect of power on wall temperature is predicted reasonably well.

In Fig. 11, we demonstrate the effect of low-to-moderate flow rates on the predicted and measured wall temperatures for Runs 441, 448, and 366. These runs were performed at the same pressure, inlet subcooling, and power but at different mass fluxes, varying from 50 to 201 kg/m^{2}s. The measured data indicate that the wall temperatures in the test section decrease with increasing flow rate at the inlet. This trend is predicted reasonably well by the model. It seems that the wall temperatures in the hot-patch region are under-predicted at low flow rates. This under-prediction gradually decreases with increasing flow rate. The flow regimes in the three runs expand slightly with increasing flow rate. The rates of increase in wall temperatures in the post-agitated regions are in good agreement with the experimental da: except in Run 448, which shows slightly slower rates at the end of the test section. It is clear from this figure that at a power level of 1.68 kW, the effect of flow rate on axial wall temperature is well predicted.

The effect of flow rate is investigated further in Fig. 12 for the moderate-to-high range of flow rate and corresponding higher power. The test section gross power was increased to 2.8 kW, whereas the flow rate was varied from 202 kg/m^{2}s to 2004 kg/m^{2}s for Runs 364, 379, and 412. The slope of the wall-temperature profile for Run 379 agrees well with the data, with wall temperatures under-predicted by 25°C. For Runs 364 and 412, the wall-temperature profiles and their slopes agree with the measured data at lower elevations but show some differences at the end of the tube. The wall temperatures in the hot-patch region also are under-predicted at very high flow rates (Run 412) as it was in the case of low flow rates. It should be noted that we have not previously assessed the model using runs with flow rates as high as 2004 kg/m^{2}s. It is evident from the figure that the prediction of axial wall temperatures is quite reasonable for such high mass fluxes.

Thus, it can be concluded that the effect of flow rate on axial wall temperature is predicted reasonably well for a large range of flow rates and powers. The effect of flow rate on predicted and measured void fractions will be considered in the future when tabulated data become available in the open literature.

In the following paragraph, we try to estimate the statistical variation in predicted wall and vapor temperatures for all of the runs listed in Table I. The wall temperature profiles indicated that the agreement or disagreement between predicted and measured values was varying as a function of the axial distance. Therefore, the predicted wall temperatures at three elevations are plotted against the measured wall temperatures for the 20 steady-state post-CHF runs. The disagreement between the predicted and measured values is greater at the exit of the hot patch, where the rough-wavy or agitated IAFs generally occur, and at the exit of the tube. Therefore, the comparisons given in Figs. 13–15 are given for axial elevations of Z = 0.2 m (the exit of hot patch), Z = 0.51 m (roughly the middle of the test tube), and Z = 0.91 m (upstream of the upper hot patch). The standard and average deviations in Figs. 13–15 are defined as follows.

$$\text{av dev} = \frac{1}{N} \sum_{i=1}^{N} \left| \left[\frac{T_{mea} - T_{cal}}{T_{mea} - T_{sat}} \right]_i \right| \qquad (2)$$

$$\text{std dev} = \left\{ \frac{1}{N} \sum_{i=1}^{N} \left[\frac{T_{mea} - T_{cal}}{T_{mea} - T_{sat}} \right]_i^2 \right\}^{1/2} \qquad (3)$$

Thus, these represent average and standard deviations for superheat and are we believe more meaningful numbers than a comparison of the absolute temperature would be.

As indicated in Fig. 13 and Table IV, the average and standard deviations of the predicted wall superheats at the elevation of 0.2 m were calculated to be 8.2% and 9.7%, respectively. As this elevation is at the end of the hot patch, all temperatures were around 800 K. The average and standard deviations at Z = 0.51 m (Fig. 14) are 10.9% and 14.3%, respectively. At Z = 0.91 m (Fig. 15), they are 11.9%

TABLE IV
STATISTICAL RESULTS FOR WINFRITH DATA IN PREDICTING WALL AND VAPOR TEMPERATURES (NUMBER OF DATA POINTS = 20)

	Wall Temperature			Vapor Temperature
Elevation (Z)	0.2 m	0.51 m	0.91 m	1.155 m
av dev	0.082	0.108	0.119	0.376
std dev	0.097	0.143	0.152	0.392

and 15.2%, respectively. These statistical values indicate that the thermal-hydraulic model gives very reasonable results in predicting wall temperatures along the test tube. At this time we could perform the assessment work for only a limited number of runs. Although the number of runs used in Figs. 13–15 may not be enough for a meaningful statistical analysis, the runs were selected to represent the typical extremes of the Winfrith post-CHF data bases found in the references (7,11). Thus, it is expected that the values reported above for the average and standard deviations will be very typical or even worse-case if more data points are used.

The overall results for predictions of vapor temperature are presented in Fig. 16. The number of data points shown in the figure is 14, not 20, because the vapor temperature could not be measured in runs with mass fluxes higher than 200 kg/m^{2}s. The systematic under-prediction of vapor temperature is clear, but the magnitude of the under-prediction is not significantly high in comparison with the uncertainty in the vapor temperature measurements (about 30°C). The average and standard deviations of the vapor superheat are 37.6% and 39.2%, respectively.

B. Assessment of the model with Berkeley Reflood Data

The Berkeley reflood test facility (11) consisted of a 3.6576-m-long Inconel 600 alloy tube with an inside diameter of 14.4 mm and a wall thickness of 0.76 mm. The reflood tests were performed at atmospheric pressures. The data include the temporal variation of wall temperature at various axial locations, the quality of steam at the tube exit, the input power to the tube, the inlet and outlet fluid temperatures, and the heat losses to the surroundings. A more detailed description of the test facility and the tabulated data can be found in Ref. 14. The TRAC model of this facility was simple and consisted of a VESSEL component, two PIPE components, a BREAK component, and a FILL component. The vessel component was one-dimensional and included 24 axial levels with a node size of 0.1524 m. The FILL component simulated the constant water injection to the test tube, and the BREAK component simulated the outlet pressure boundary conditions. The heat losses from the test tube to the surroundings were given using a temperature-dependent heat-transfer coefficient in Ref. 11. A special update considering this temperature-dependent heat-transfer coefficient was used in the TRAC code for the heat losses.

A series of eight Berkeley reflood tests was chosen for this assessment work. The operating parameters of selected tests are given in Table V.

TABLE V
BERKELEY TRANSIENT REFLOOD TESTS USED FOR THE INDEPENDENT ASSESSMENT OF THE MODEL

Run No.	G (kg/m^2s)	$Q_{electric}$ (W)	P (bar)	T_{in} (C)
166	23.6	1172	1.0	25.0
167	71.0	1172	1.0	23.3
177	23.8	1201	1.0	61.7
186	117.5	1145	1.0	23.3
188	72.0	3687	1 0	25.6
192	165.4	8899	1.0	17.8
193	116.3	8880	1.0	19.4
194	72.0	8917	1.0	20.0

These tests were selected to investigate the effect of the mass flow rate, power, and inlet fluid temperature on the thermal hydraulic characteristics of the test tube undergoing reflood quench. Note that the electrical power is listed in Table V and it does not include the heat losses.

Figure 17 shows the calculated and measured wall temperature histories at five different measurement (thermocouple) locations (0.61 m, 1.372 m, 1.83 m, 2.44 m,and 3.05 m from the inlet of the test section for Run 166. The predicted wall temperature at the 0.61 m starts to decrease slightly early. However, the predicted rate of decrease in wall temperature agrees with measured data very well, indicating that the precursory cooling rate at this location is predicted very well. At higher elevations, the decrease in wall temperatures in the prediction starts a few seconds later than data. This is more profound at axial elevations of 2.44 and 3.05 m. The predicted precursory cooling rates at all elevations are in good agreement with measured data. This results are reasonable, but increasingly late, prediction of the quench time at each axial location.

The average quench-front velocity (rewetting velocity) between thermocouple locations can be calculated by dividing the axial distance between these locations by the time required for the quench front to move from one location to another. However, this requires the definition of the quench time of a particular location. Unal (12) defined the quench time of a given location as the time when the rate of wall temperature decrease was greatest. This criterion gave a wall superheat of 200°C at atmospheric pressures. The quench time of a given location in this work was defined when the wall superheat was about 400 K. The predicted and measured average rewetting velocities are shown in Fig. 18 for Runs 166, 167, and 186. The predicted rewetting velocity between 0–0.61 m is in reasonable agreement with measured data for Run 166. It is under-predicted between 0.61 m and 1.372 m. At higher elevations, both the predicted and measured rewetting velocities indicate a decreasing-increasing-decreasing trend and agree with each other reasonably well. It can be concluded that the rewetting velocity and its variation with axial distance are predicted reasonably well for the conditions of Run 166.

When the mass flux is increased while the other variables (electrical power, inlet fluid temperature, and initial wall temperature) are kept constant, one could expect that the time required to quench a particular axial location should decrease. This trend is shown in Fig. 19, where the predicted and measured wall temperature histories of the five different axial locations for Run 167 are presented. In Run 167, the mass flux is increased to 71 kg/m^{2}s. The rate of wall temperature decrease in predicted values is slightly greater than the measured data. This results in an early, but reasonable, prediction of the rewetting velocities along the tube as shown in Fig. 18. Comparing Figs. 17 and 19 clearly shows that an increase in the mass flow rate causes an increase in the rate of wall temperature decrease (indicating that the precursory cooling rate is increased). This results in a decrease in quench times and correspondingly an increase in rewetting velocities as seen in Fig. 18.

The effect of mass flux is investigated further in Fig. 20, which shows Run 186. Run 186 was performed with the same power, inlet temperature, and initial wall temperatures as those used in Runs 166 and 167, but the mass flux was increased to 117.5 kg/m^{2}s. The decrease in the quench time and an increase in the rate of wall temperature decrease at each thermocouple location are evident. Also, it is clear that the predicted and measured wall temperature histories are again in reasonable agreement. The predicted and measured rewetting velocities also increase with increasing mass flux as shown in Fig. 17.

Runs 166, 167, and 186 were conducted with relatively low test section powers. The electrical power input corresponds to a heat flux level of about 0.7 W/cm^2 (heat losses are not included). One can conclude from the above discussion that the model is expected to predict the history of the thermal-hydraulic conditions in channels undergoing reflood well for the relatively low heat flux and moderate mass flux ranges.

Generally, rewetting velocity decreases with an increase in wall heat flux. In Figs. 21 and 22, we show that the model developed in Ref. 1 predicts this trend. Figure 21 shows the predicted and measured wall temperature histories for Run 188. The calculated and measured rewetting velocities along the test tube are plotted in Fig. 22 for this run. Run 188 uses the same operating conditions as Run 167 except that the test section power is increased by factor of 3 (3687 W). Comparing Fig. 18 and Fig. 22 indicates that the predicted rewetting velocities decreases when the heat flux is increased and also that they are in good agreement with measured data. The predicted variation of the rewetting velocity along the test tube agrees with the measured data. The wall-temperature histories at all thermocouple elevations are predicted reasonably as shown in Fig. 21. However, an oscillatory behavior in the wall temperature is evident in this run and is found to have a more profound effect at the higher elevations.

It is our experience that for relatively high heat fluxes, the expansion and collapse of the inverted annular flow regimes can occur in the prediction because of the relatively fast variation in the predicted void fraction prediction (associated with the increased amount of vapor generation and an associated increase interfacial drag coefficient). This causes the oscillations in wall temperature as seen in Fig. 21. For these relatively high heat fluxes, this oscillatory behavior is expected to become more profound (see Ref. 13). Although the hydrodynamic parameters such as void fraction, pressure, etc. could oscillate in reflood experiments, their frequency is generally high enough not to effect the wall temperature behavior. The measured rewetting velocity decreases with increasing axial distance as shown in Fig. 22. It is under-predicted at lower elevations and over-predicted at higher elevations. It is clear that further improvements are needed in the thermal-hydraulic model for very high heat flux boundary conditions.

When the mass flux is increased at the same heat flux level (Run 192 shown as Fig. 24 in comparison with Run 193 shown as Fig. 23), the wall temperature oscillations are damped. The calculated and measured rewetting velocities are plotted as a function of the axial distance in Fig. 22. For this run, the calculated values followed the measured trend, but their magnitudes were smaller.

The calculated rewetting velocities between thermocouple locations for all Berkeley reflood runs considered in this work are plotted against the measured data in Fig. 25. Although the number of data points was not high enough to produce meaningful statistical numbers for the 37 data points used in Fig. 23, the average and standard variations were found to be 26% and 40%, respectively, showing very reasonable predictions.

IV. SUMMARY AND CONCLUSIONS

Based on this work, the following conclusions can be drawn.

1. The thermal-hydraulic model gave reasonable predictions of the Winfrith post-CHF void fractions and their variation with axial distance. The relative error between predicted and measured void fractions was 10% at locations far downstream of the post-agitated IAF for a pressure range of 2–10 bar and a heat flux range of 3.6–8.03 W/cm^2. Just downstream of the post-agitated IAF, the predictions deviate by about 40% from the measured values. These errors were systematic for all the runs considered. The predictions improve for lower pressures and higher heat fluxes. The effects of pressure and power on the void fraction and its variation with axial distance were predicted correctly. The effect of pressure is more apparent than the effect of heat flux.
2. The hot-patch model was capable of modeling the Winfrith steady-state post-CHF experiments. It predicted reasonable energy input to coolant from the bottom hot patch and did not allow any quench-front propagation from either the bottom or top. The transient calculations converged to steady-state conditions in relatively short times for the conditions of the Winfrith tests studied in this work. The calculated thermal-hydraulic parameters at 250 s were used for steady-state post-CHF data-model comparisons.
3. Among the five runs selected to assess the hot-patch model, the average deviation in predicting the hot-patch power was 15.4%, indicating reasonable agreement. This type of energy imbalance produces minor changes in the equilibrium quality at the inlet of the test tube; for Run 451 (which shows the maximum disagreement), the equilibrium quality at the exit of the hot patch (no conduction downstream of the hot patch is considered) is 1.7% if the calculated hot patch power is used and 2.3% if the measured hot patch power is used. A change this small in inlet quality is not expected to change the thermal response of the wall significantly.

Therefore, the hot-patch power predicted by the model is reasonable and is expected to be so for other ranges of parameters.

4. The effects of pressure and test section power on axial wall temperature for Winfrith post-CHF data are predicted reasonably well for steady-state data. The wall temperatures along the tube elevation seem to be over-predicted for lower pressures and under-predicted for higher pressures by about 50°C.
5. The effect of flow rate on axial wall temperature is predicted reasonably well for a large range of flow rates for steady-state Winfrith data.
6. A comparison of the predicted and measured wall superheats at the beginning, middle, and end of the test tube for 20 Winfrith steady-state post-CHF tests indicated that the maximum average deviation in the predictions was 15.2% .
7. The vapor superheats for the Winfrith steady-state data were systematically under-predicted, and the average deviation was 37.6% for 14 data points.
8. The predicted wall-temperature histories show reasonable agreement for most of the Berkeley transient reflood tests used in this work, indicating reasonable prediction of overall wall and interfacial heat transfer. The agreement was very good for relatively low heat fluxes. At high heat fluxes, the wall temperature trace showed some oscillations that were not shown in the experimental data. Further improvements are needed for high-heat-flux conditions, where the vapor generation rate could be high; the current interfacial drag model may not consider the correct void fraction effect, allowing the void fraction to change drastically and causing low-frequency oscillations in calculations. Experimental information aimed at defining it and at-what-power such oscillations occur would be very useful.
9. The predicted rewetting velocity and its variation along the test tube was in reasonable agreement with measured data for all Berkeley runs. The overall comparison of predicted and measured data indicated an average deviation of 26% and a standard deviation of 40%. These values are considered to be reasonable.

We believe from the above comparisons that the thermal-hydraulic reflood model used in TRAC/PF1-MOD2 gives reasonable global results in predicting void fraction, wall temperature, and their variation with tube axial distance for Winfrith steady-state post-CHF data bases. It is expected that assessment results also will be reasonable for any other steady-state post-CHF data base or any other Winfrith steady-state post-CHF test. The model also gave satisfactory global results in predicting the Berkeley reflood test data except for high-heat-flux conditions where some disagreement between predicted and measured data existed.

Although they are not formulated as mechanistic models, the formulation of the near-wall liquid effect and the transition boiling models gave reasonable results in predicting wall-to-fluid heat transfer and quench-front propagation. There is a need for further work for the axial-dependent transition boiling model and the near-wall liquid effects. The results discussed in this paper indicate that the capillary and vapor Reynolds numbers defined at the CHF point could be the proper dimensionless numbers for the modeling transition boiling. The vapor Reynolds number also determines the near-wall liquid contribution. The functional form of this contribution indicates that it should increase gradually up to the agitated IAF, become maximum in the agitated IAF, and finally diminish with axial distance in the post-agitated regime.

As a result of the above-mentioned shortcomings and the fact that we have not discussed details of the various predictions that has lead us to characterize our results as being satisfactory on a "global" basis. The results discussed in this paper are presented in the hope of aiding future development of improved mechanistic models for prediction of post-CHF conditions dealing with the quenching of heated structures. In particular, work is needed in the area of the history-dependent transition boiling model, the near-wall liquid effect, the unheated-wet-wall effect, and the IAF interfacial drag models, wall and interfacial heat transfer, and interfacial drag coefficient models at high heat fluxes.

V. REFERENCES

1. R. A. Nelson and C. Unal, "A Phenomenological Model of Thermal-Hydraulics of Convective Boiling During the Quenching of Hot Rod Bundles; Part I: Thermal-Hydraulic Model," submitted for the possible presentation in National Heat Transfer Conference in 1991.

2. C. Unal, K. Tuzla, C. A. Tuzla, and J. C. Chen, "Vapor Generation Model for Dispersed Drop Flow," 1989 National Heat Transfer Conference, ANS Proceedings HTC-Vol. 4, August 6-9, 1989.

3. K. Hirano et al., "Data Report on Large Scale Reflood Test-14, CCTF Test CI-5 (Run 014)," JAERI memo 57-214 (August 1982).

4. D. Swinnerton, M. L. Hood, and K. G. Pearson, "Steady-State Post-Dryout at Low Quality and Medium Pressure Data Report," Winfrith United Kingdom Atomic Energy Authority report AEEW-R 2267 (June 1988).

5. K. Tuzla, C. Unal, O. Badr, S. Neti, and J. C. Chen, "Thermodynamic Nonequilibrium in Post-Critical-Heat-Flux Boiling in a Rod Bundle," US Nuclear Regulatory Commission report NUREG/CR-5095, Volumes 1–4 (July 1987).

6. R. A. Nelson and C. Unal, "A Phenomenological Model of Thermal-Hydraulics of Convective Boiling During the Quenching of Hot Rod Bundles," Los Alamos National Laboratory report in preparation.

7. C. Unal, K. Tuzla, and J. Chen, "A TRAC-PF1/MOD1 Analysis of a Lehigh Rod Bundle Post-CHF Reflood Test," Lehigh University Institute of Thermo-Fluid Engineering and Science report TS-861 (July 1986).

8. C. Unal, K. Tuzla, O. Badr, S. Neti, and J. C. Chen, "Convective Boiling in a Rod Bundle: Transverse of Vapor Superheat Temperature Under Stabilized Post-CHF Conditions," Los Alamos National Laboratory document accepted by the Int. J. Heat Mass Trans. (1990).

9. C. Unal, K. Tuzla, O. Badr, S. Neti, and J. C. Chen, "Convective Film Boiling in a Rod Bundle: Axial Variation of Evaporation Ratio," Int. J. Heat and Mass Trans. **31**, 2091 (October 1988).

10. D. Swinnerton, R. A. Savage, and K. G. Pearson, "Heat Transfer Measurements in Steady-State Post-Dryout at Low Quality and Medium Pressure," AEA Thermal Reactor Services, Physics and Thermal Hydraulic Division report AEA-TRS-1045, Winfrith United Kingdom Atomic Energy report AEEW-R 2503 (April 1990).

11. R. Seban et al., "UC-B Reflood Program: Experimental Data Report," EPRI report NP-743, Research Project 248-1 (April 1978).

12. C. Unal, "An Experimental Study of Thermal Non-Equilibrium Convective Boiling in Post-Critical-Heat-Flux Region in Rod Bundles," Ph.D. Thesis, Lehigh University (1985).

13. C. Unal, E. Haytcher, R. A. Nelson, "A Phenomenological Model of Thermal Hydraulics of Convective Boiling During the Quenching of Hot Rod Bundles Part II; Model Assessment Using Winfrith Steady-State Post-CHF Void Fraction and Heat Transfer Measurements and Berkeley Transient Reflood Test Data," Los Alamos National Laboratory document submitted to Nuc. Eng. and Design.

Figure Captions

Fig. 1. The calculated wall surface temperature histories at eight different axial elevations for Winfrith Run 176

Fig. 2. Predicted and measured lower hot-patch powers for Runs 176, 446, 451, 448, and 434

Fig. 3. Predicted axial void fraction and IFDC profiles and measured void fraction data for Winfrith steady-state Run 434.

Fig. 4. The effect of system pressure on the predicted and measured axial void fraction profiles.

Fig. 5. Predicted axial void fraction and IFDC profiles and measured void fraction data for Winfrith steady-state Run 446.

Fig. 6. The effect of test section power on the predicted and measured axial void fraction profiles.

Fig. 7. The calculated and measured wall and vapor temperatures for Winfrith Runs 176 and 179.

Fig. 8. The predicted wall-to-liquid and wall-to-vapor heat fluxes as a function of test section height for Winfrith Run 176.

Fig. 9. The effect of system pressure on the predicted and measured axial wall temperature profiles.

Fig. 10. The effect of test section power on the predicted and measured axial wall temperature profiles.

Fig. 11. The effect of flow rate on the predicted and measured axial wall temperature profiles at a test section power of 1.68 kW.

Fig. 12. The effect of flow rate on the predicted and measured axial wall temperature profiles at a test section power of 2.8 kW.

Fig. 13. Predicted and measured wall temperatures at the exit of the hot patch ($Z = 0.2$ m) for 20 Winfrith steady-state post-CHF runs.

Fig. 14. Predicted and measured wall temperatures at the middle of the test tube ($Z = 0.51$ m) for 20 Winfrith steady-state post-CHF runs.

Fig. 15. Predicted and measured wall temperatures at the end of the test tube (Z = 0.91 m) for 20 Winfrith steady-state post-CHF runs.

Fig. 16. Predicted and measured vapor temperatures at the end of the test tube (Z = 1.156 m) for 14 Winfrith steady-state post-CHF runs.

Fig. 17. The predicted and measured wall temperature histories at five thermocouple locations for Berkeley Run 166.

Fig. 18. The predicted and measured average rewetting velocities between thermocouple locations for Berkeley Runs 166, 167, and 186.

Fig. 19. The predicted and measured wall temperature histories at five thermocouple locations for Berkeley Run 167.

Fig. 20. The predicted and measured wall temperature histories at five thermocouple locations for Berkeley Run 186.

Fig. 21 The predicted and measured wall temperature histories at five thermocouple locations for Berkeley Run 188.

Fig. 22. The predicted and measured average rewetting velocity between thermocouple locations for Berkeley Runs 188, 192, and 193.

Fig. 23. The predicted and measured wall temperature histories at five thermocouple locations for Berkeley Run 193.

Fig. 24. The predicted and measured wall temperature histories at five thermocouple locations for Berkeley Run 192.

Fig. 25. The predicted and measured average rewetting velocities between thermocouple locations for all Berkeley runs considered in this work.

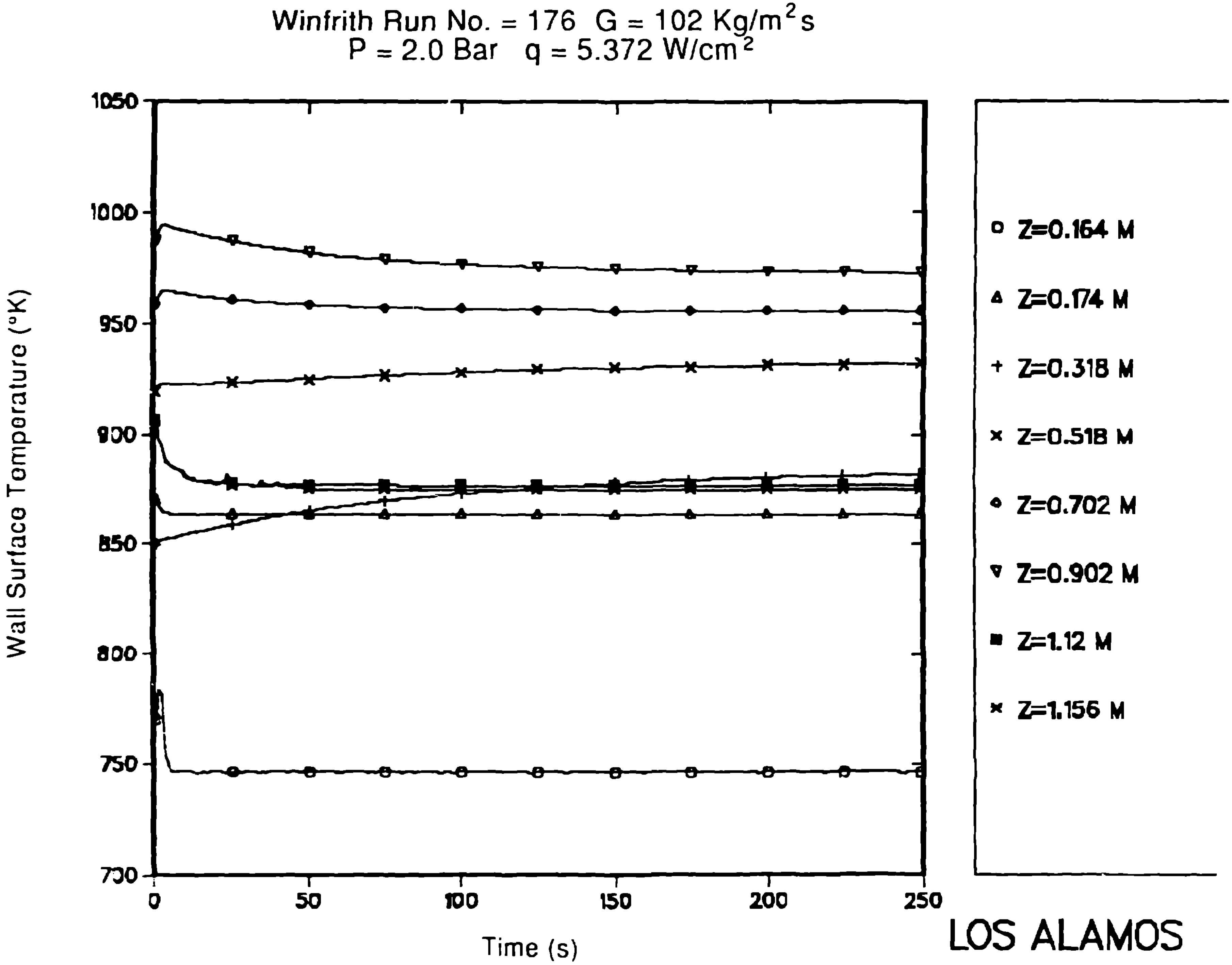

Fig. 1. The calculated wall surface temperature histories at eight different axial elevations for Winfrith Run 176

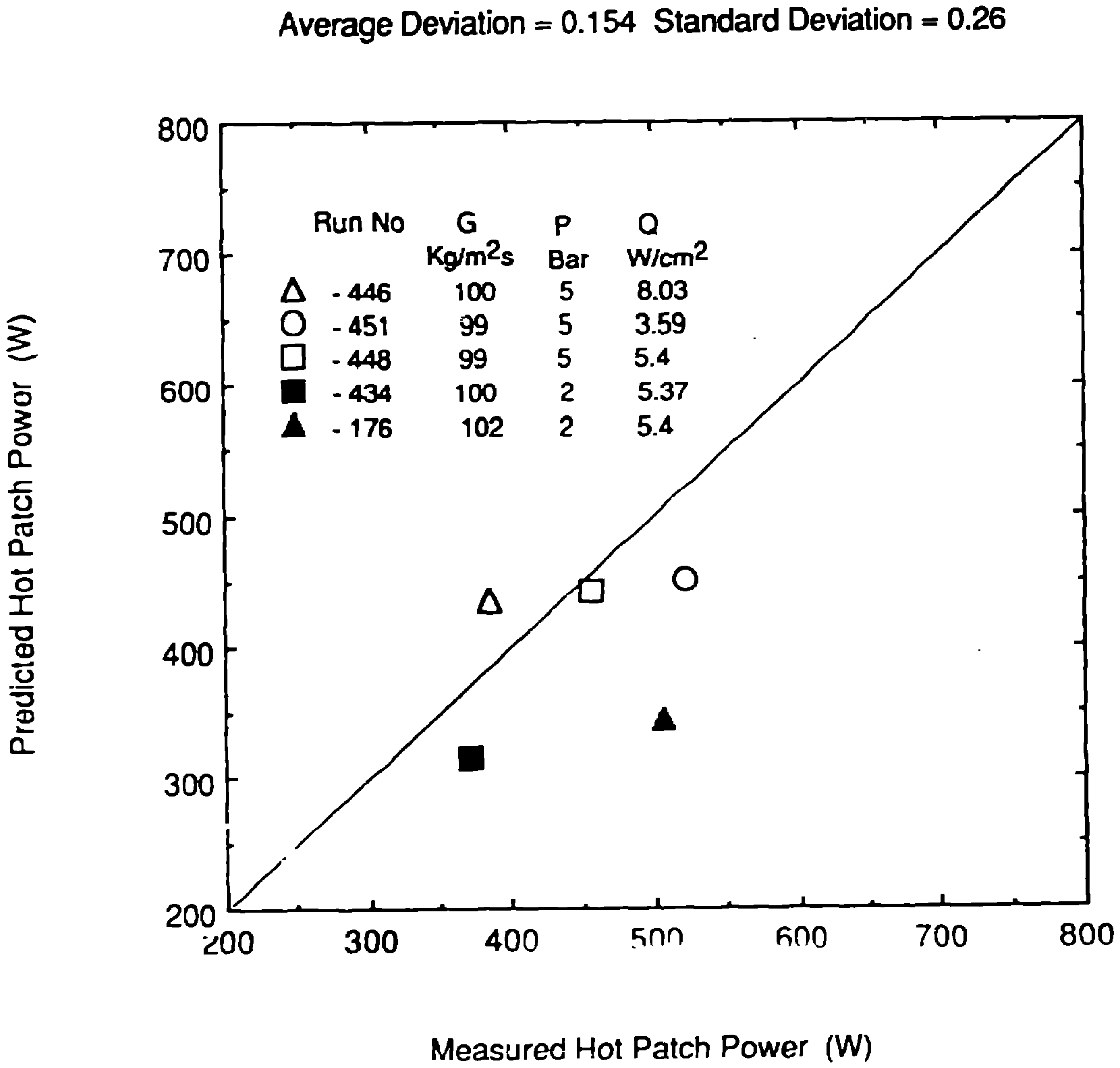

Fig. 2. Predicted and measured lower hot-patch powers for Runs 176, 446, 451, 448 and 434

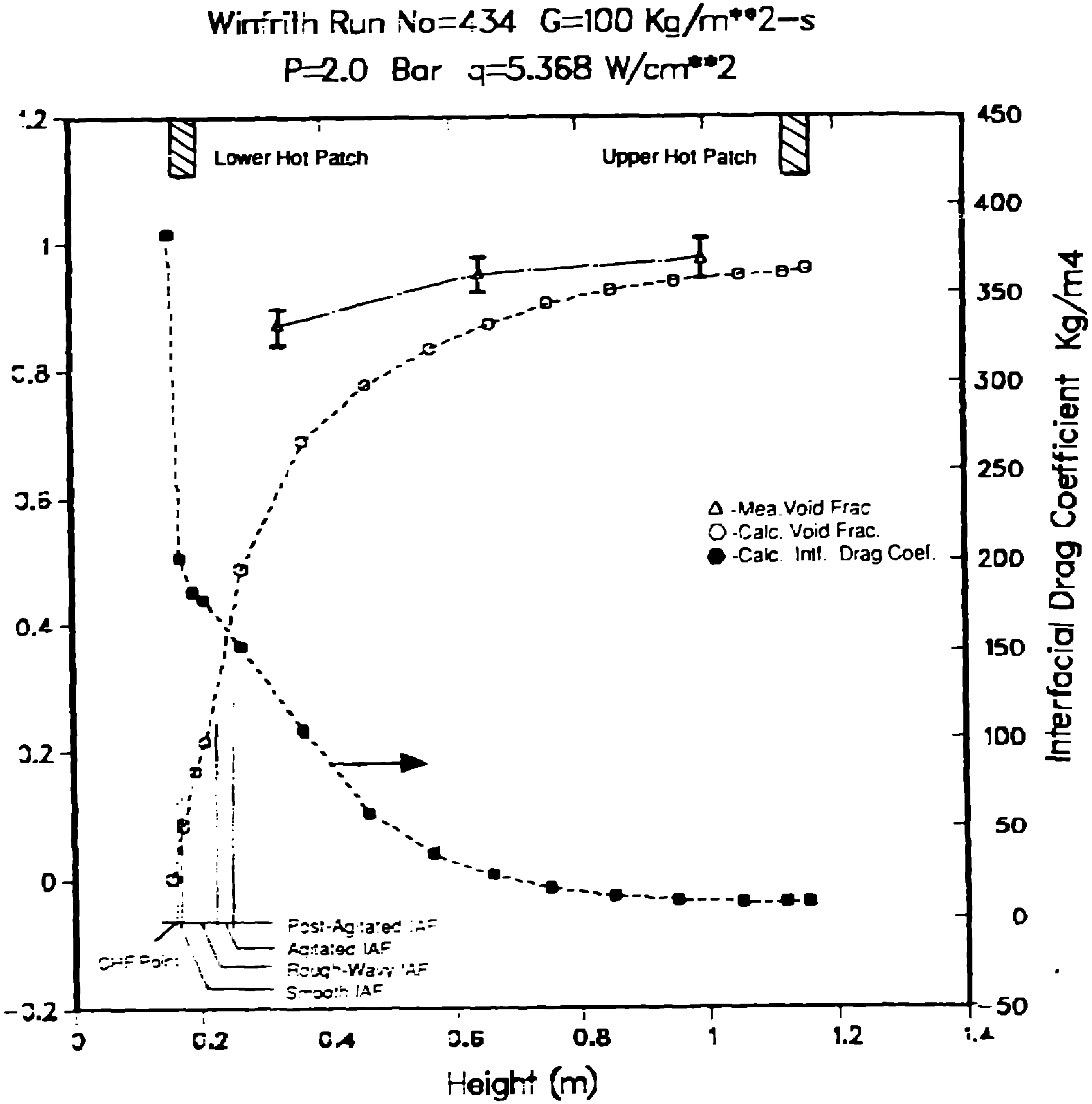

Fig. 3. Predicted axial void fraction and IFDC profiles and measured void fraction data for Winfrith steady-state Run 434.

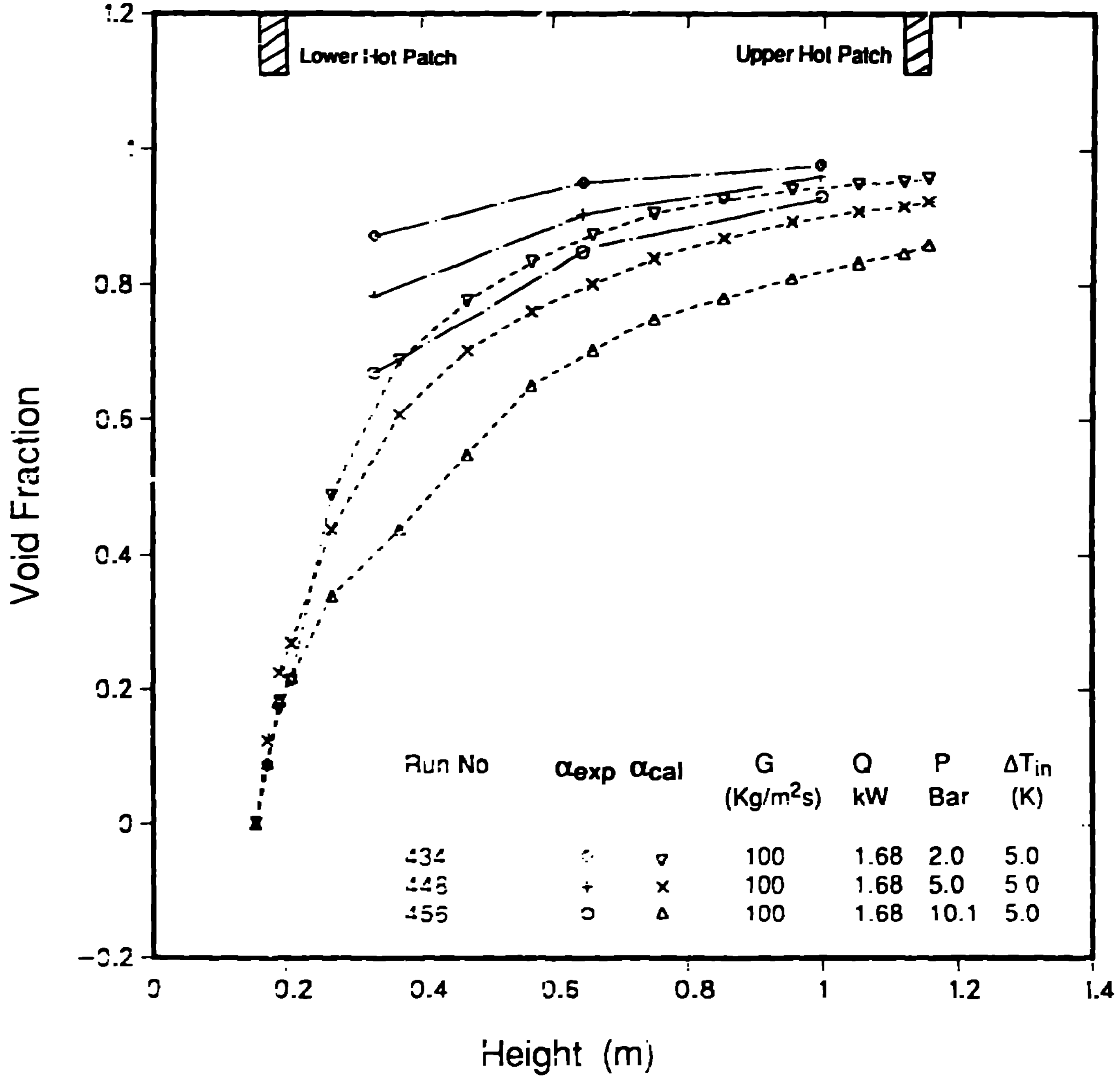

Fig. 4. The effect of system pressure on the predicted and measured axial void fraction profiles.

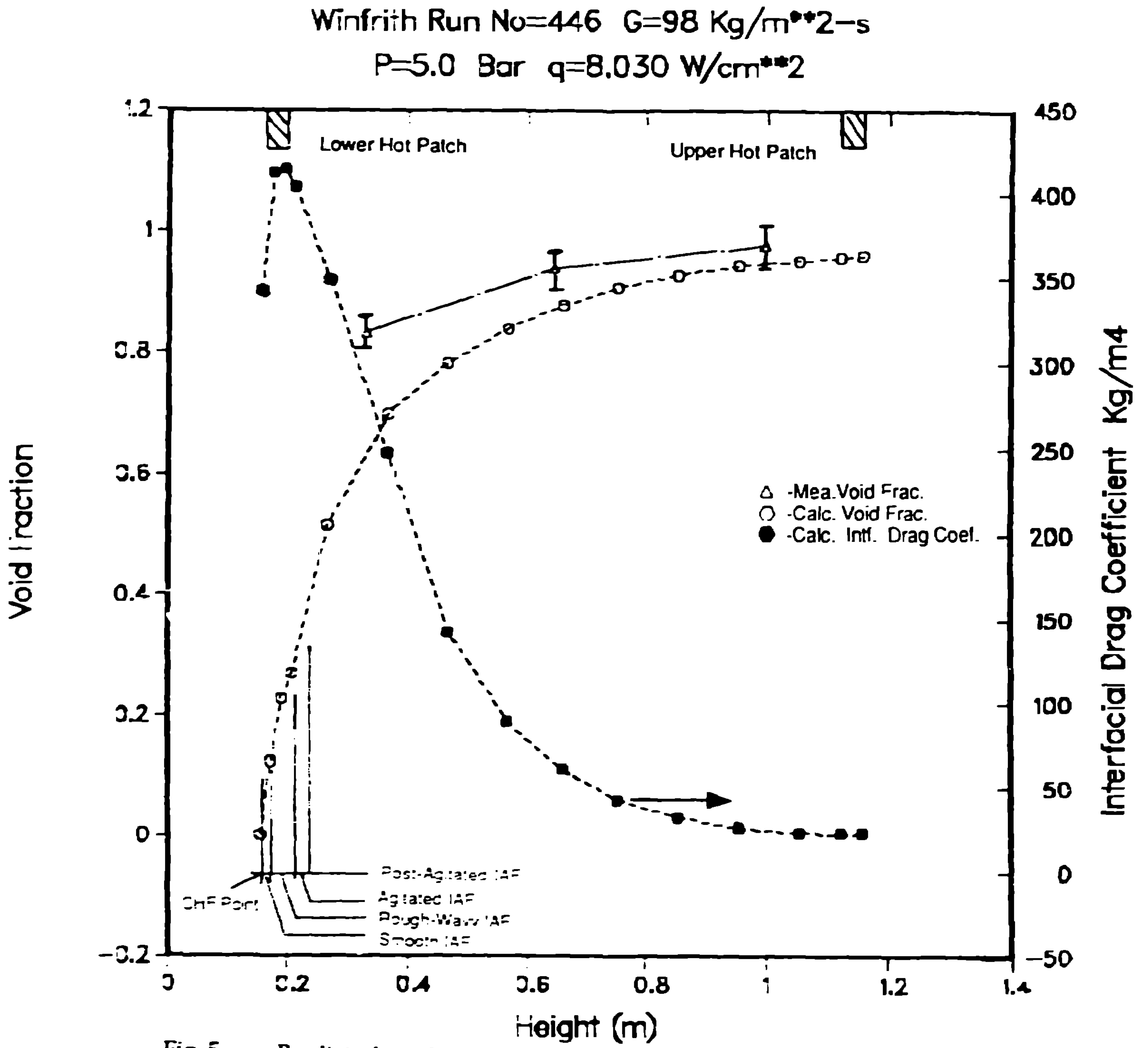

Fig. 5. Predicted axial void fraction and IFDC profiles and measured void fraction data for Winfrith steady-state Run 446.

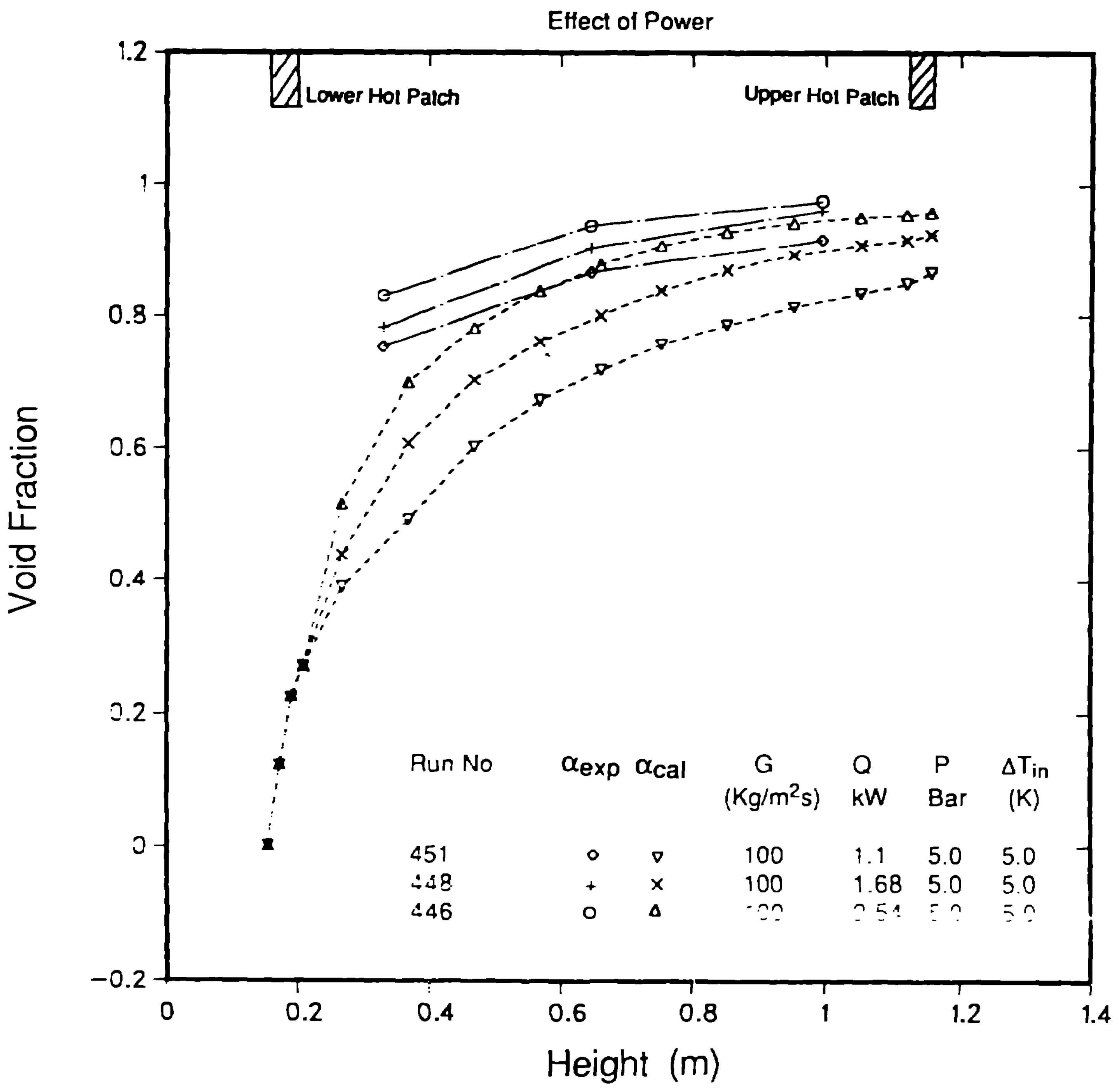

Fig. 6. The effect of test section power on the predicted and measured axial void fraction profiles.

No	°C	°C	°C	°C	Kg/m²s	Bar	W/cm²	°C
176	△	X	○	+	102	2.0	5.37	115.4
179	⊠	✱	◇	▽	103	2.01	2.40	115.4

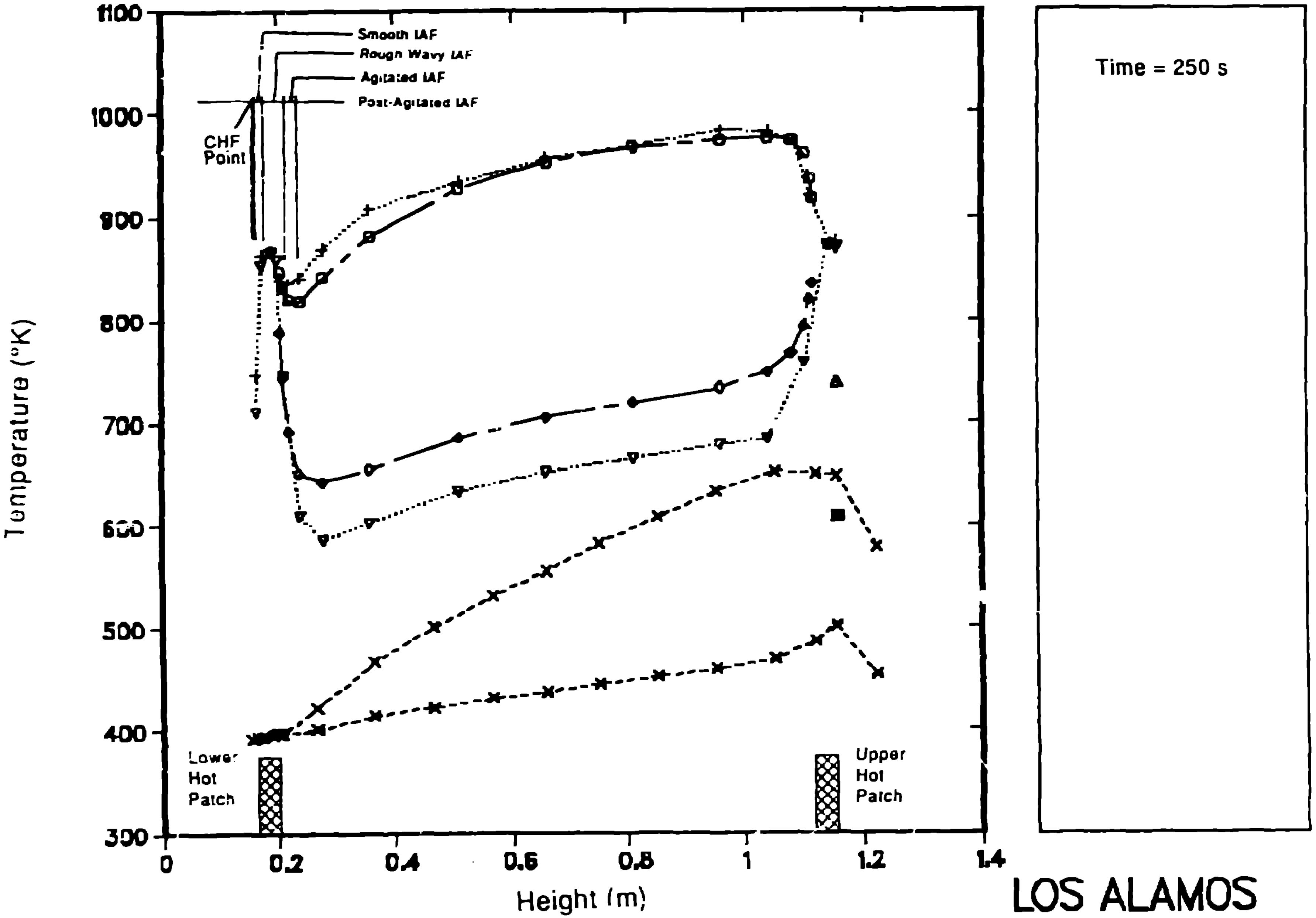

LOS ALAMOS

Fig. 7. The calculated and measured wall and vapor temperatures for Winfrith Runs 176 and 179.

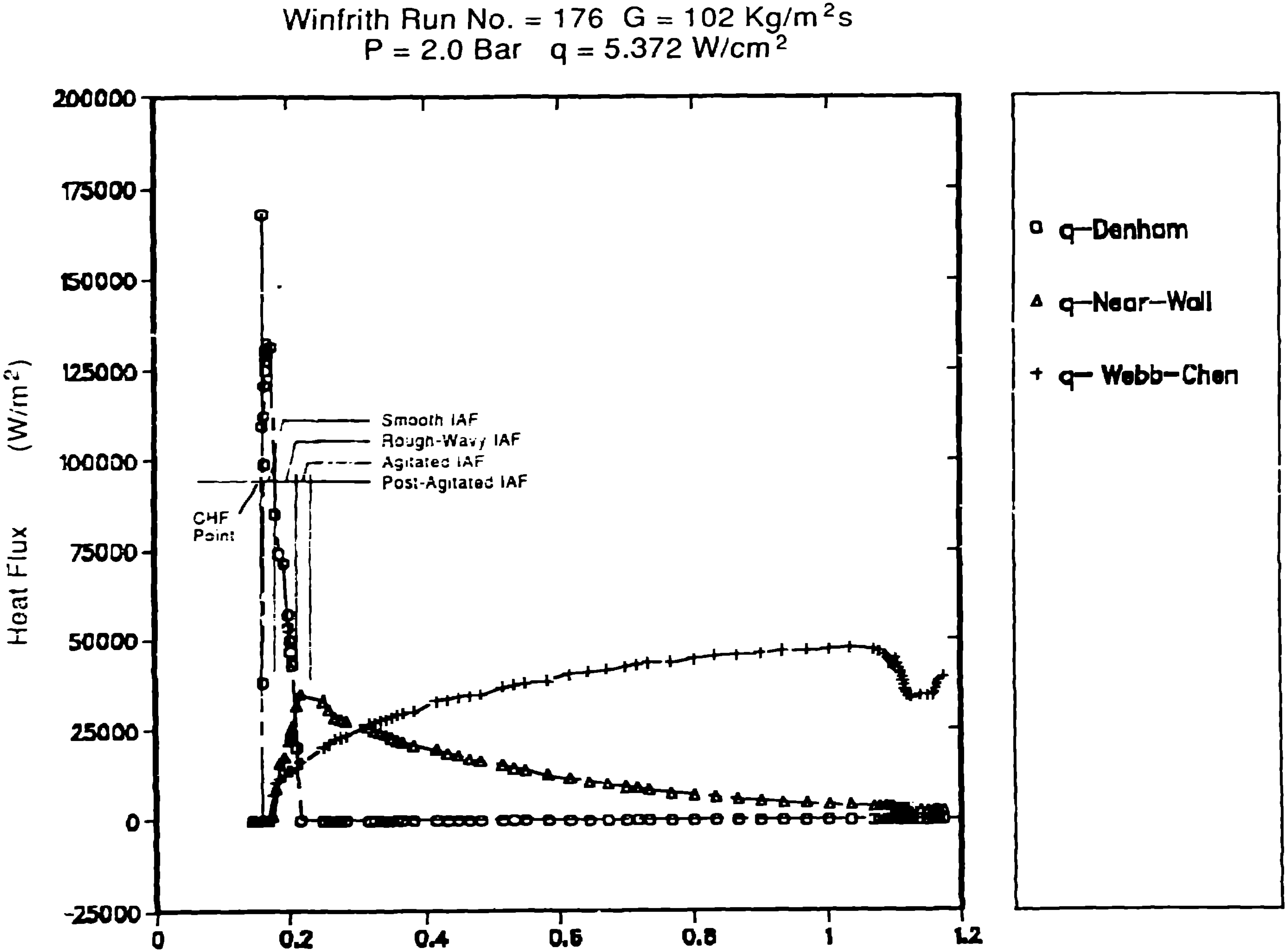

LOS ALAMOS

Fig. 8. The predicted wall-to-liquid and wall-to-vapor heat fluxes as a function of test section height for Winfrith Run 176

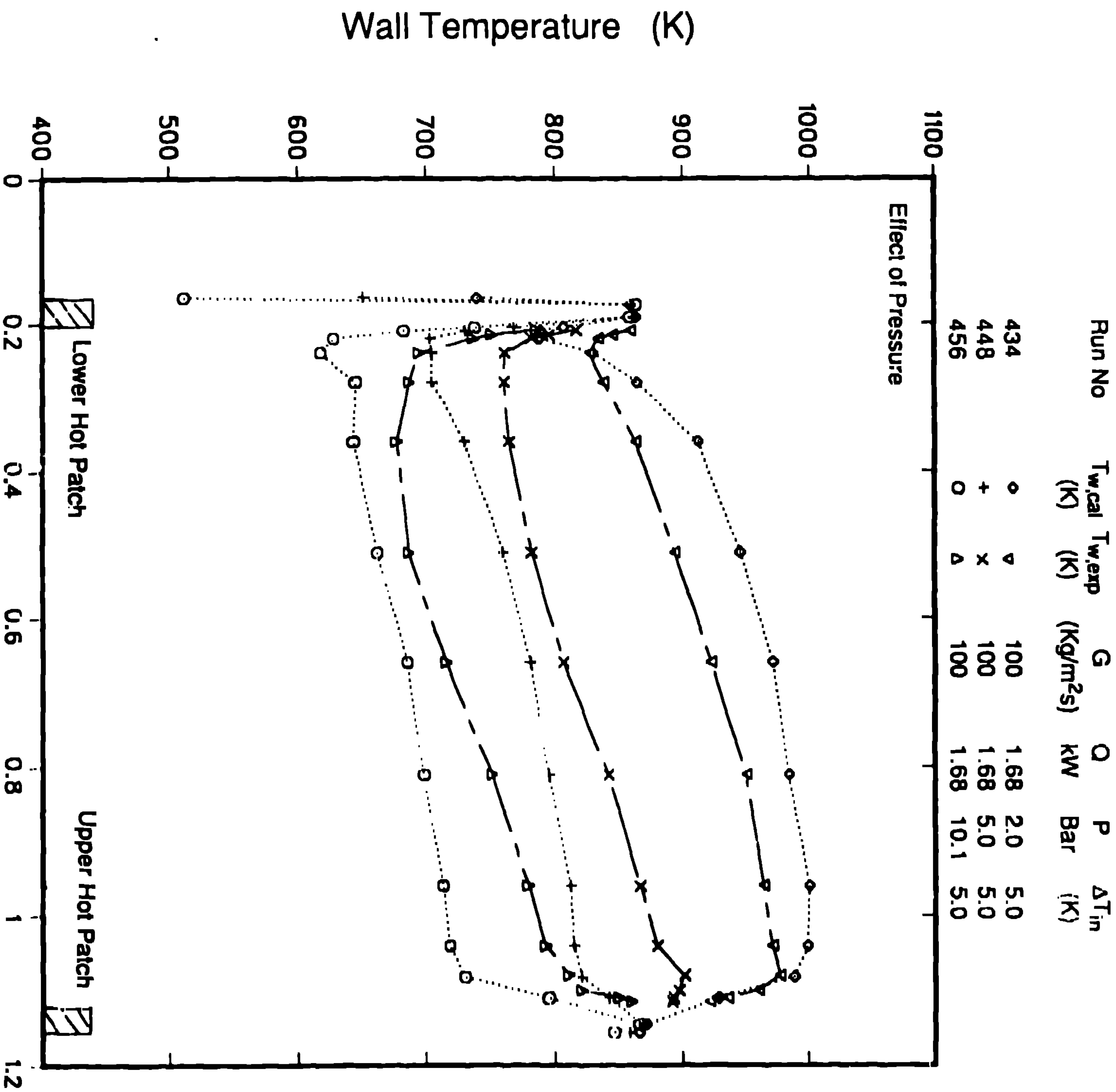

Fig. 9. The effect of system pressure on the predicted and measured axial wall temperature profiles.

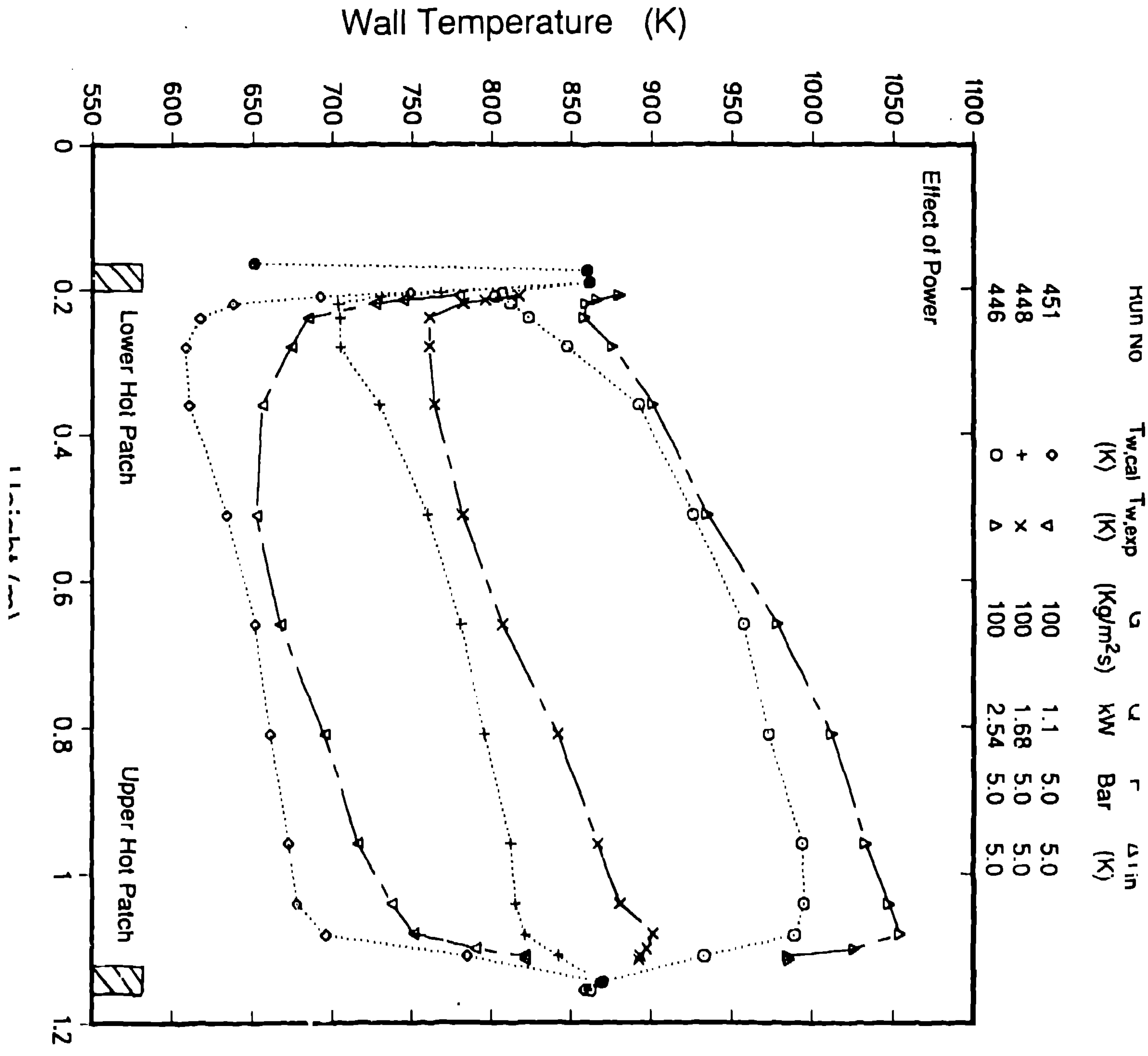

Fig. 10. The effect of test section power on the predicted and measured axial wall temperature profiles.

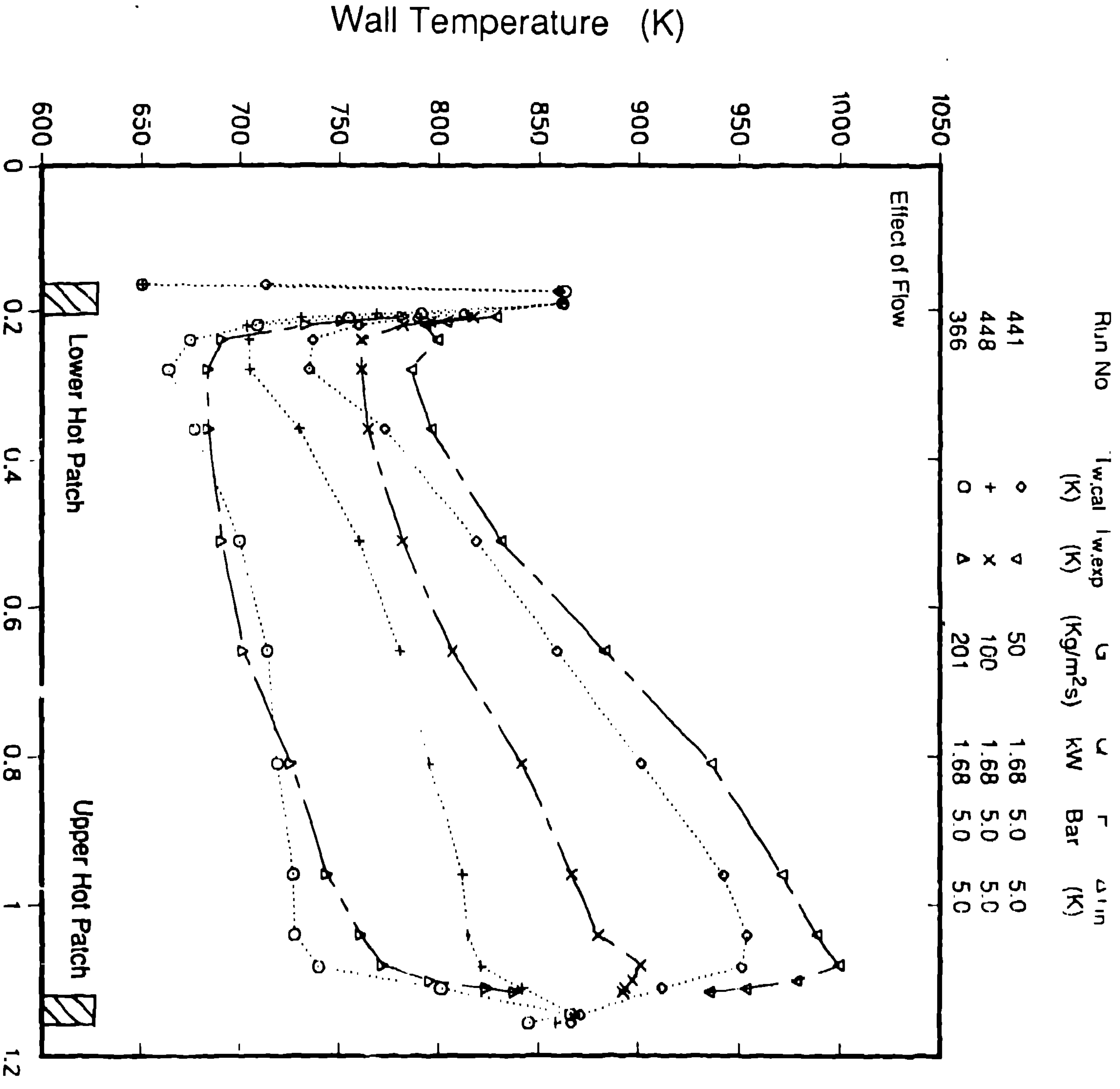

Fig. 11. The effect of flow rate on the predicted and measured axial wall temperature profiles at a test section power of 1.68 kW.

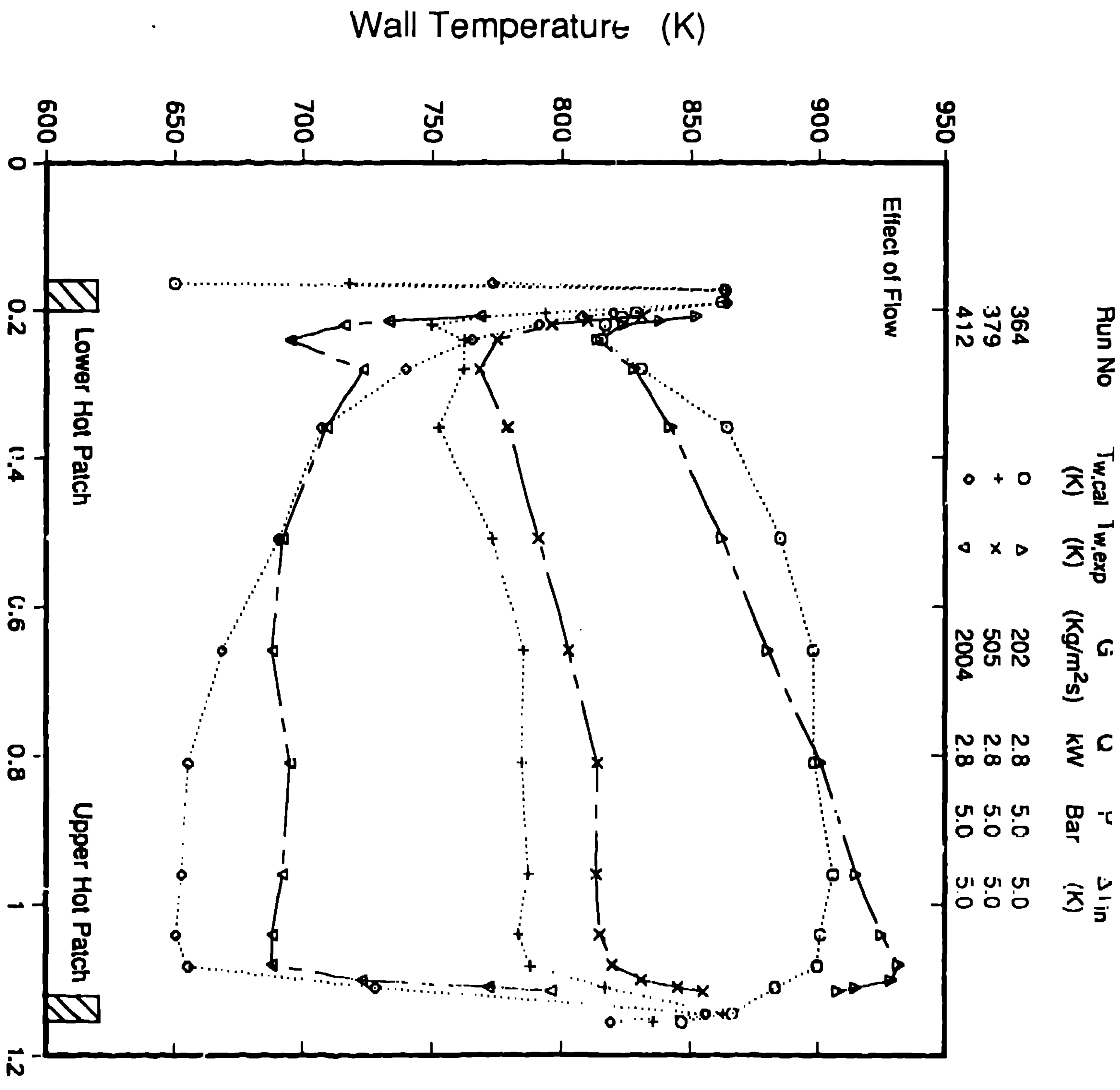

Fig. 12. The effect of flow rate on the predicted and measured axial wall temperature profiles at a test section power of 2.8 kW.

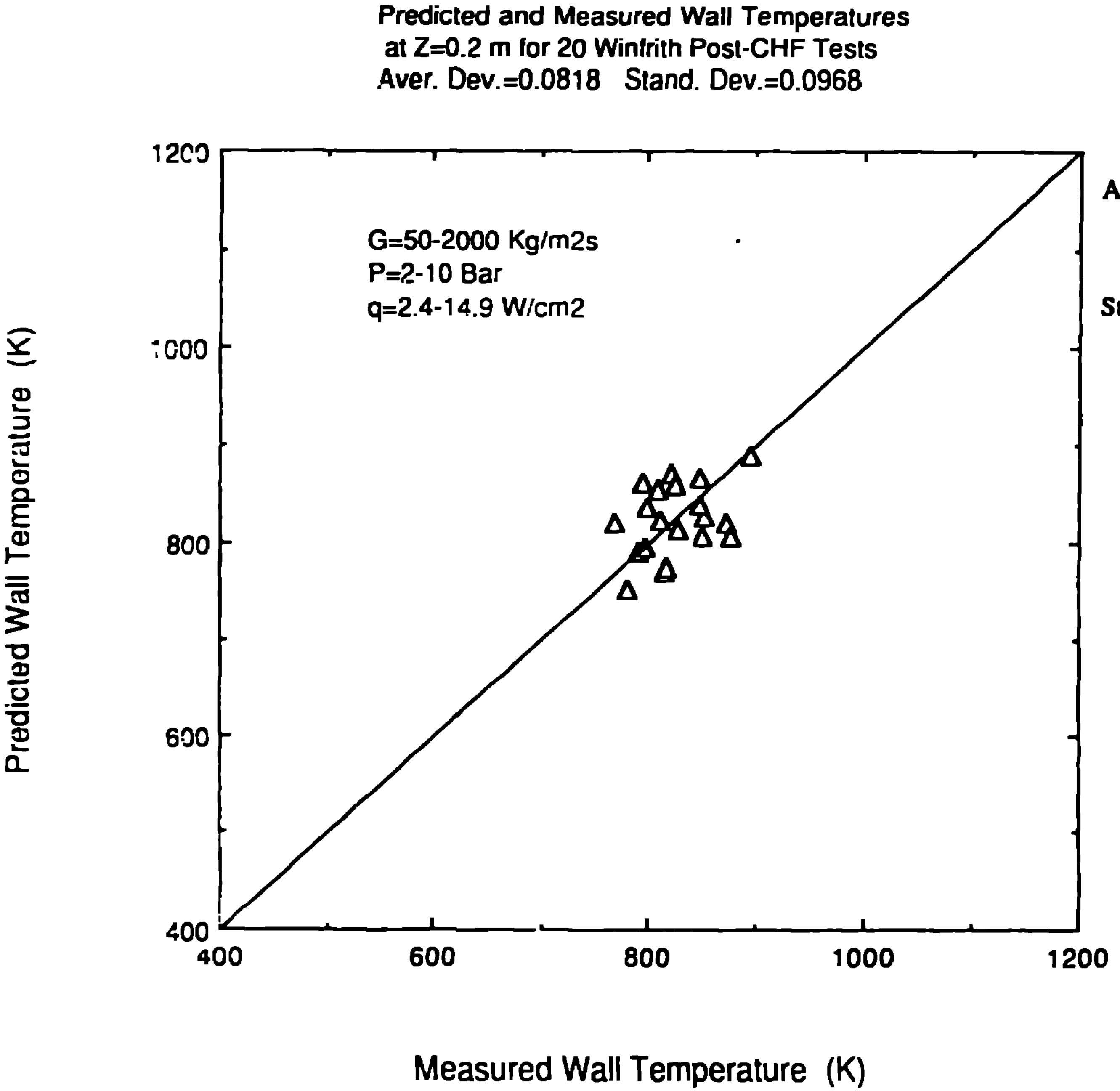

$$\text{Aver. Dev.} = \frac{1}{N}\sum_{i=1}^{N}\left[\frac{T_{mea} - T_{cal}}{T_{mea} - T_{sat}}\right]_i$$

$$\text{Stand. Dev.} = \left\{\frac{1}{N}\sum_{i=1}^{N}\left[\frac{T_{mea} - T_{cal}}{T_{mea} - T_{sat}}\right]_i^2\right\}^{1/}$$

Fig. 13 Predicted and measured wall temperatures at the exit of the hot patch (Z=0.2 m) for 20 Winfrith steady-state post-CHF runs.

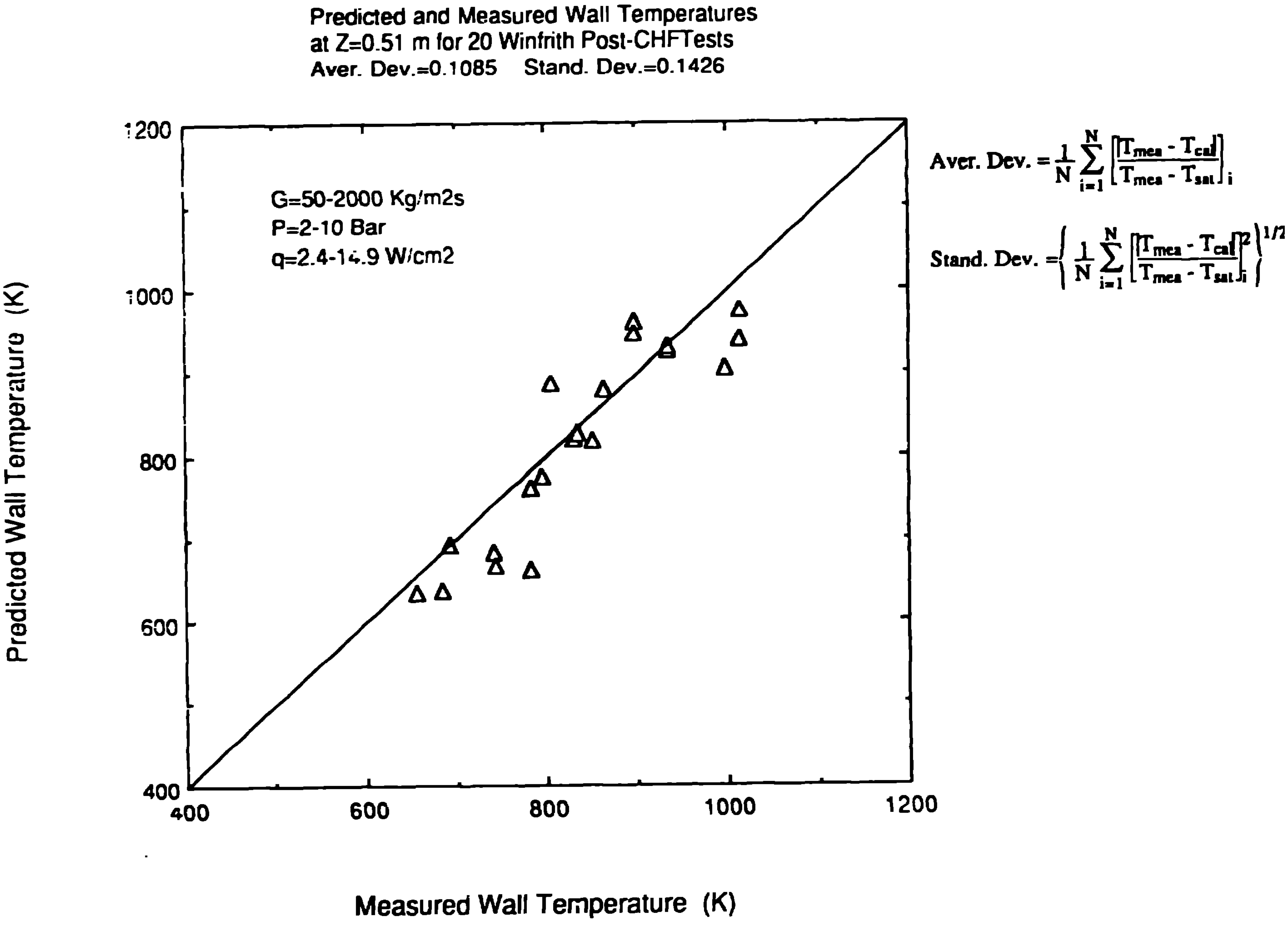

Fig. 14. Predicted and measured wall temperatures at the middle of the test tube ($Z=0.51$ m) for 20 Winfrith steady-state post-CHF runs.

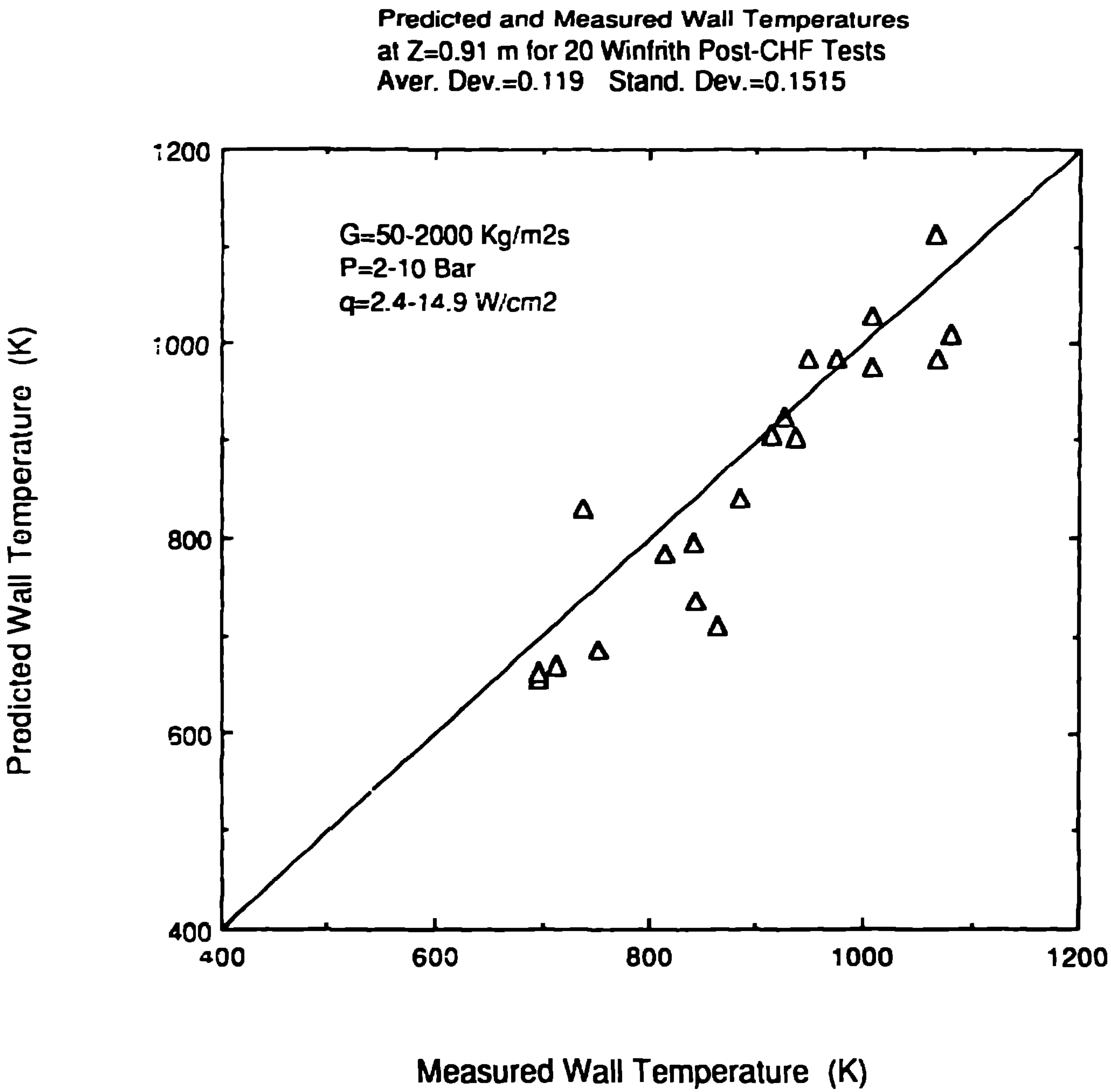

$$\text{Aver. Dev.} = \frac{1}{N}\sum_{i=1}^{N}\left[\frac{|T_{mea} - T_{cal}|}{T_{mea} - T_{sat}}\right]_i$$

$$\text{Stand. Dev.} = \left\{\frac{1}{N}\sum_{i=1}^{N}\left[\frac{|T_{mea} - T_{cal}|}{T_{mea} - T_{sat}}\right]_i^2\right\}^{1/2}$$

Fig. 15. Predicted and measured wall temperatures at the end of the test tube (Z=0.91 m) for 20 Winfrith steady-state post-CHF runs.

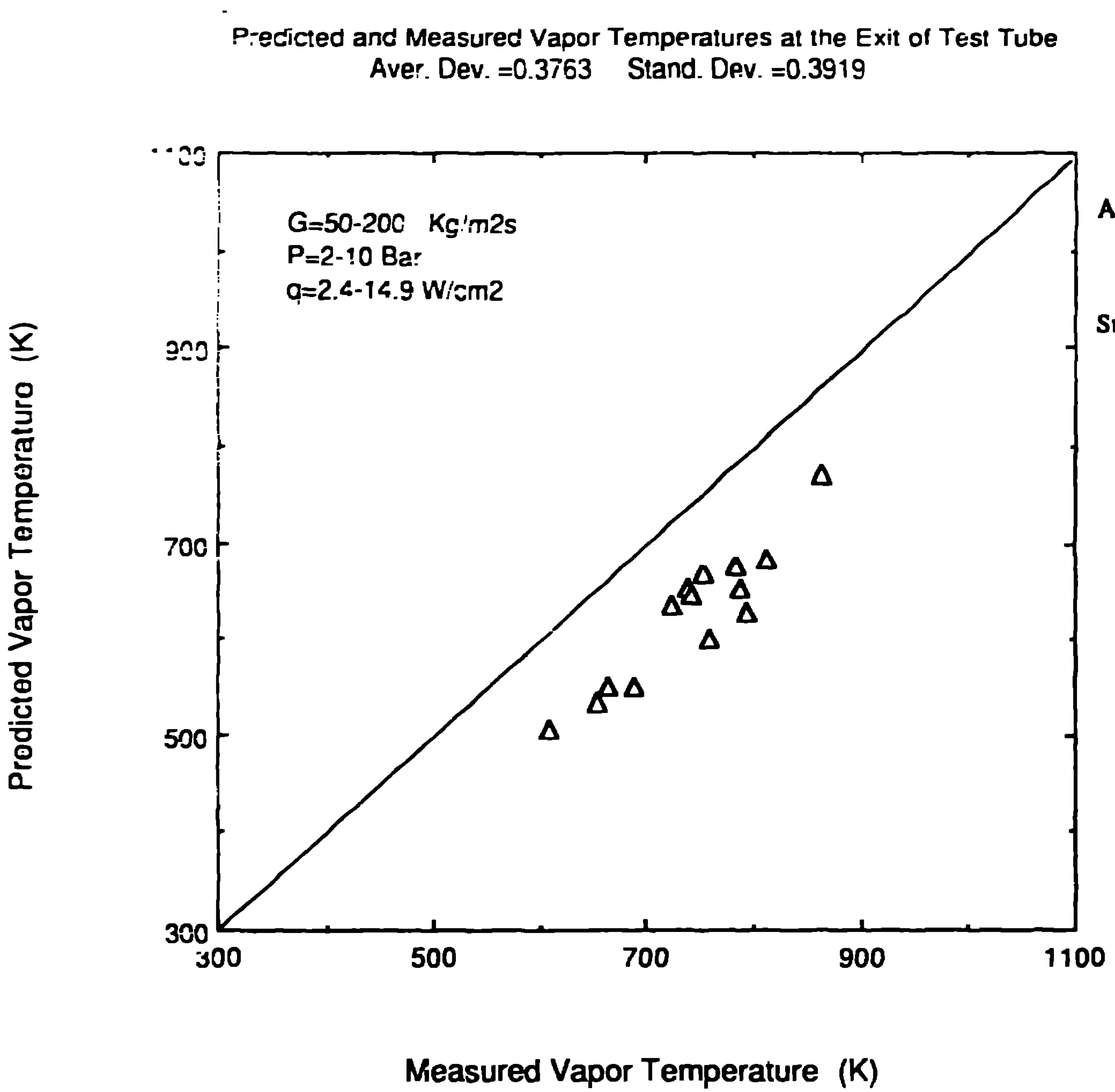

$$\text{Aver. Dev.} = \frac{1}{N}\sum_{i=1}^{N}\left[\frac{|T_{mea} - T_{cal}|}{T_{mea} - T_{sat}}\right]_i$$

$$\text{Stand. Dev.} = \left\{\frac{1}{N}\sum_{i=1}^{N}\left[\frac{|T_{mea} - T_{cal}|}{T_{mea} - T_{sat}}\right]_i^2\right\}^{1/2}$$

Fig. 16. Predicted and measured vapor temperatures at the end of the test tube (Z=1.156 m) for 14 Winfrith steady-state post-CHF runs.

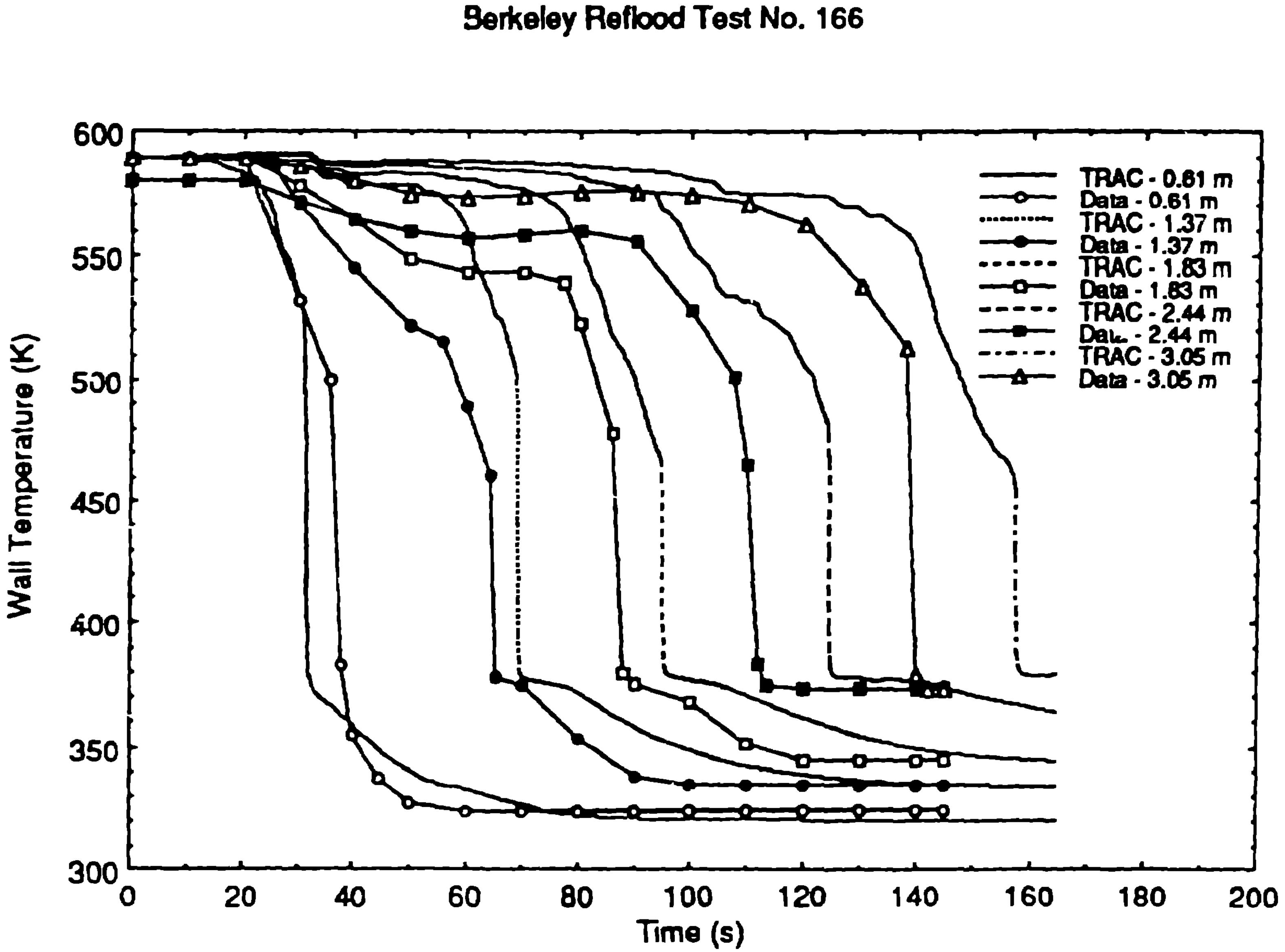

Fig. 17. The Predicted and Measured Wall Temperature Histories at Five Thermocouple Locations For Berkeley Run 166.

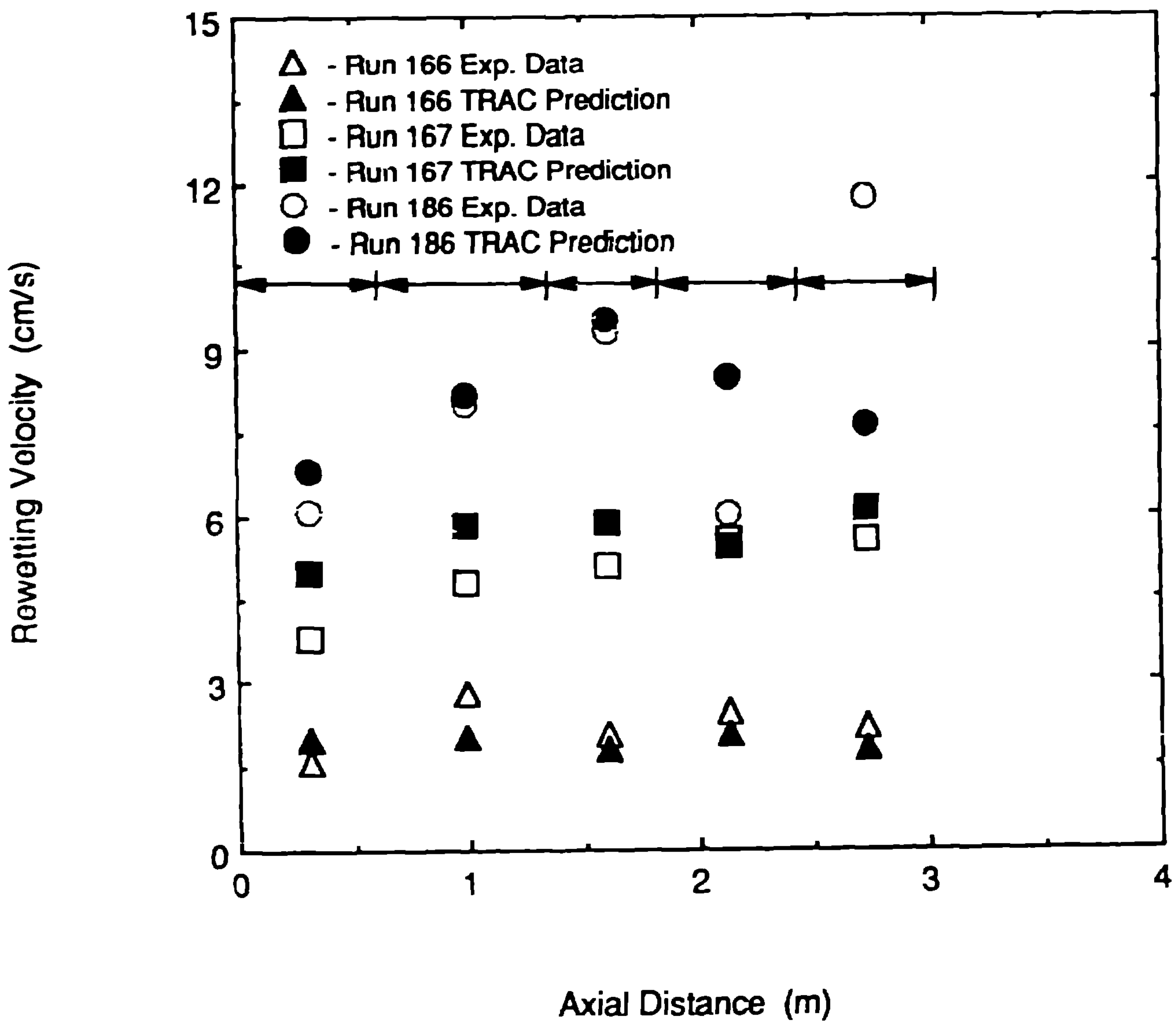

Fig. 18. The Predicted and Measured Average Rewetting Velocity Between Thermocouple Locations for Berkeley Runs 166, 167 and 186.

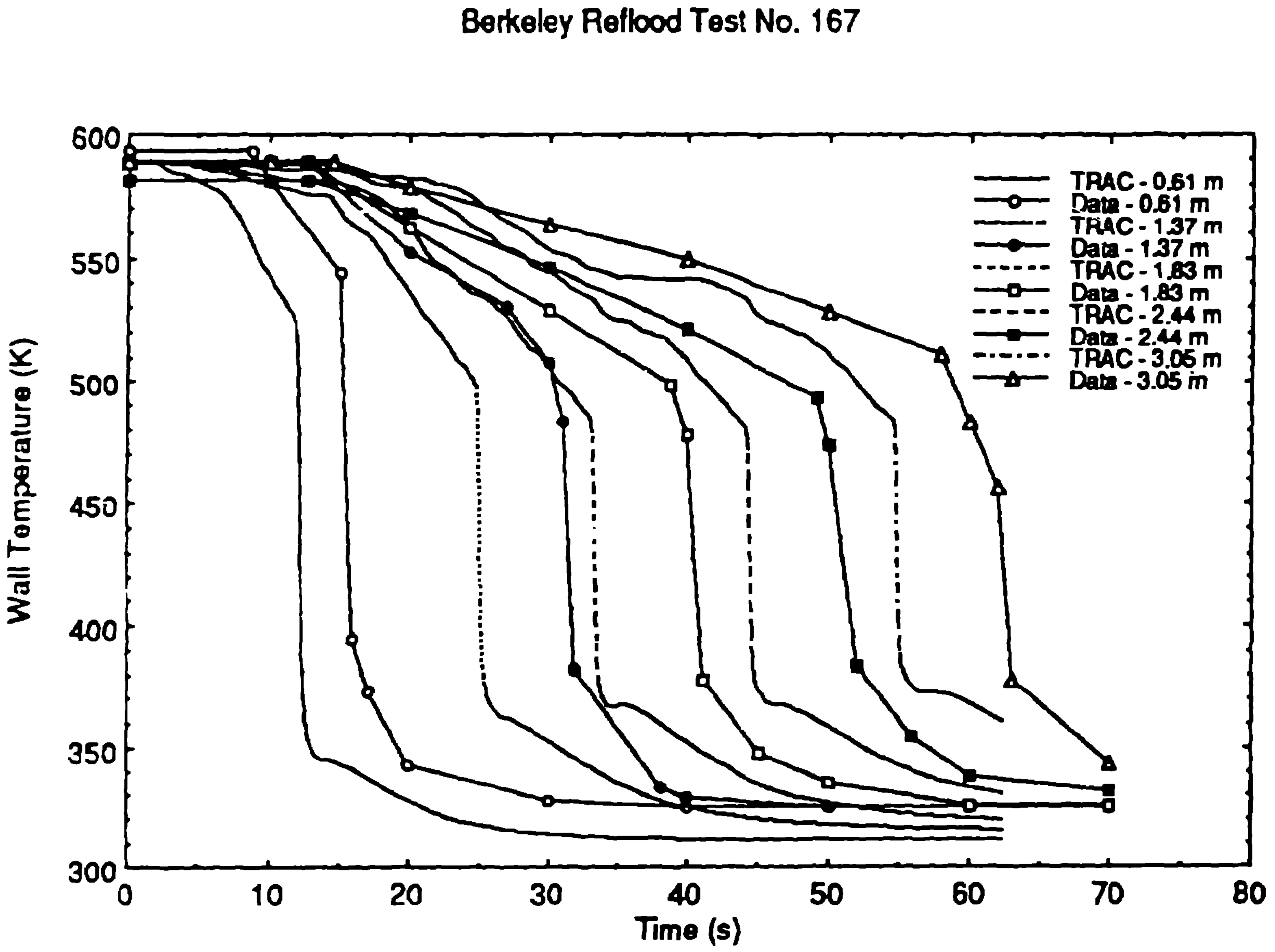
Berkeley Reflood Test No. 167

Fig. 19. The Predicted and Measured Wall Temperature Histories at Five Thermocouple Locations For Berkeley Run 167.

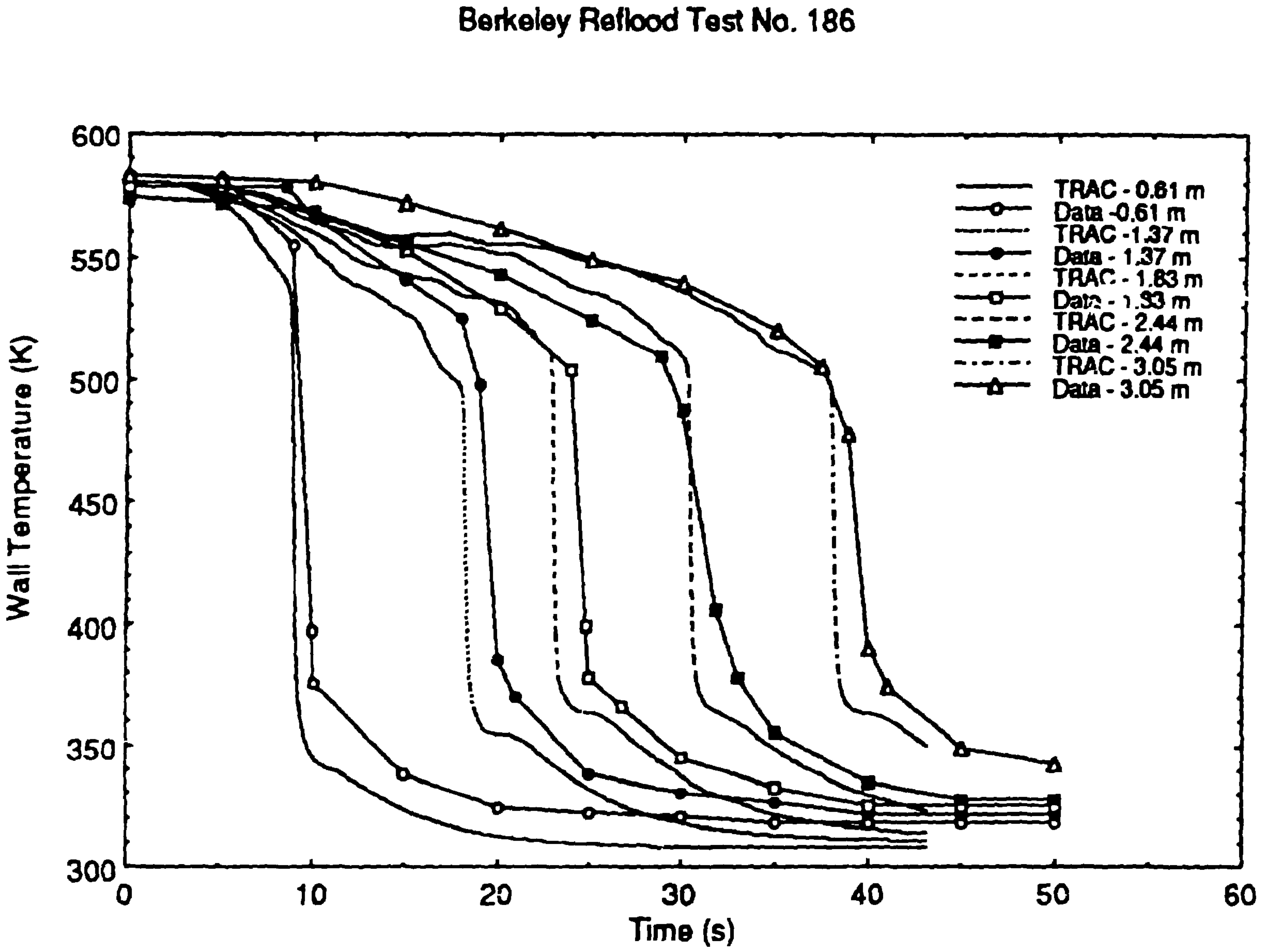

Fig. 20 The Predicted and Measured Wall Temperature Histories at Five Thermocouple Locations For Berkeley Run 186.

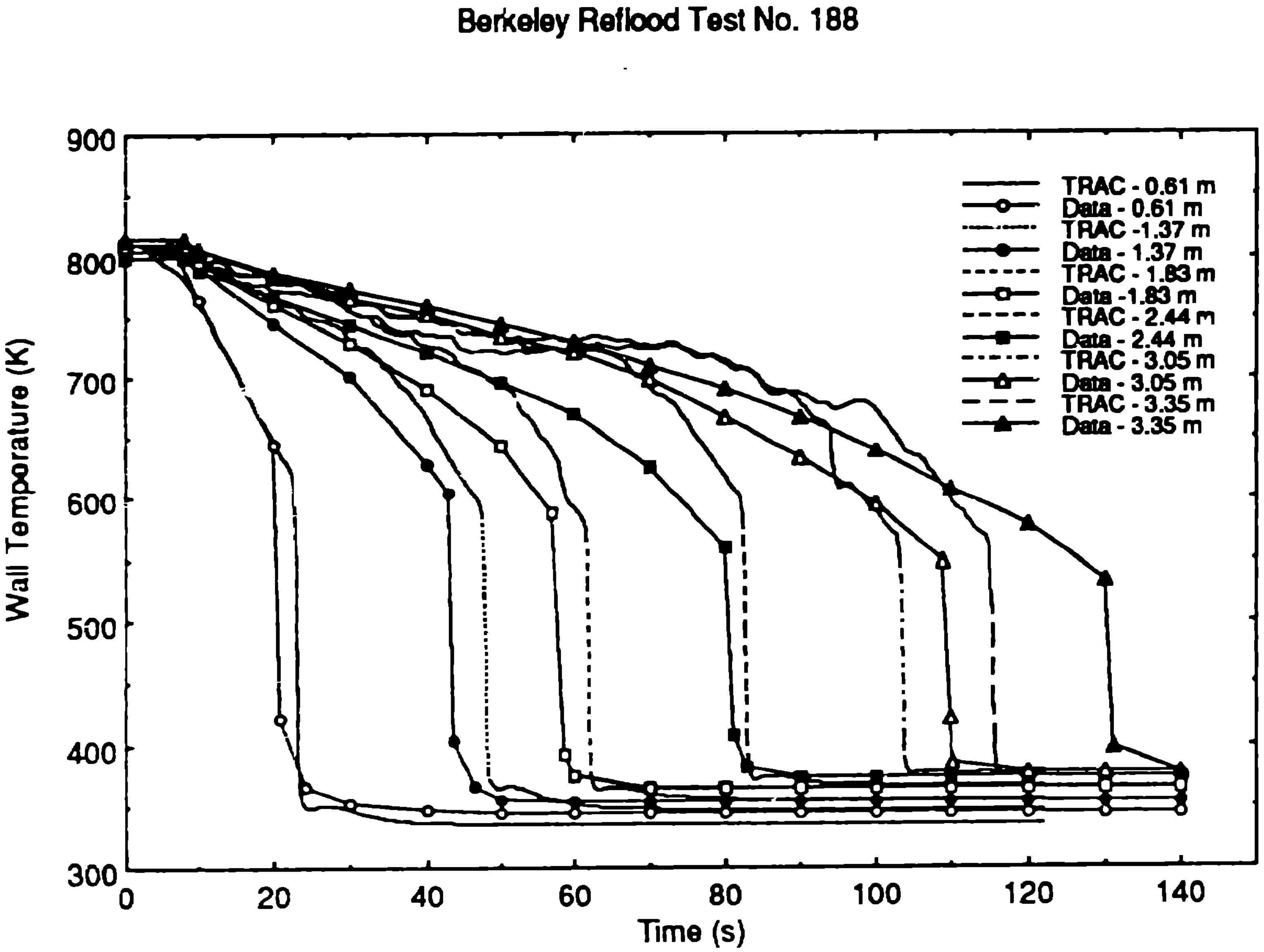

Fig. 21 The Predicted and Measured Wall Temperature Histories at Five Thermocouple Locations For Berkeley Run 188.

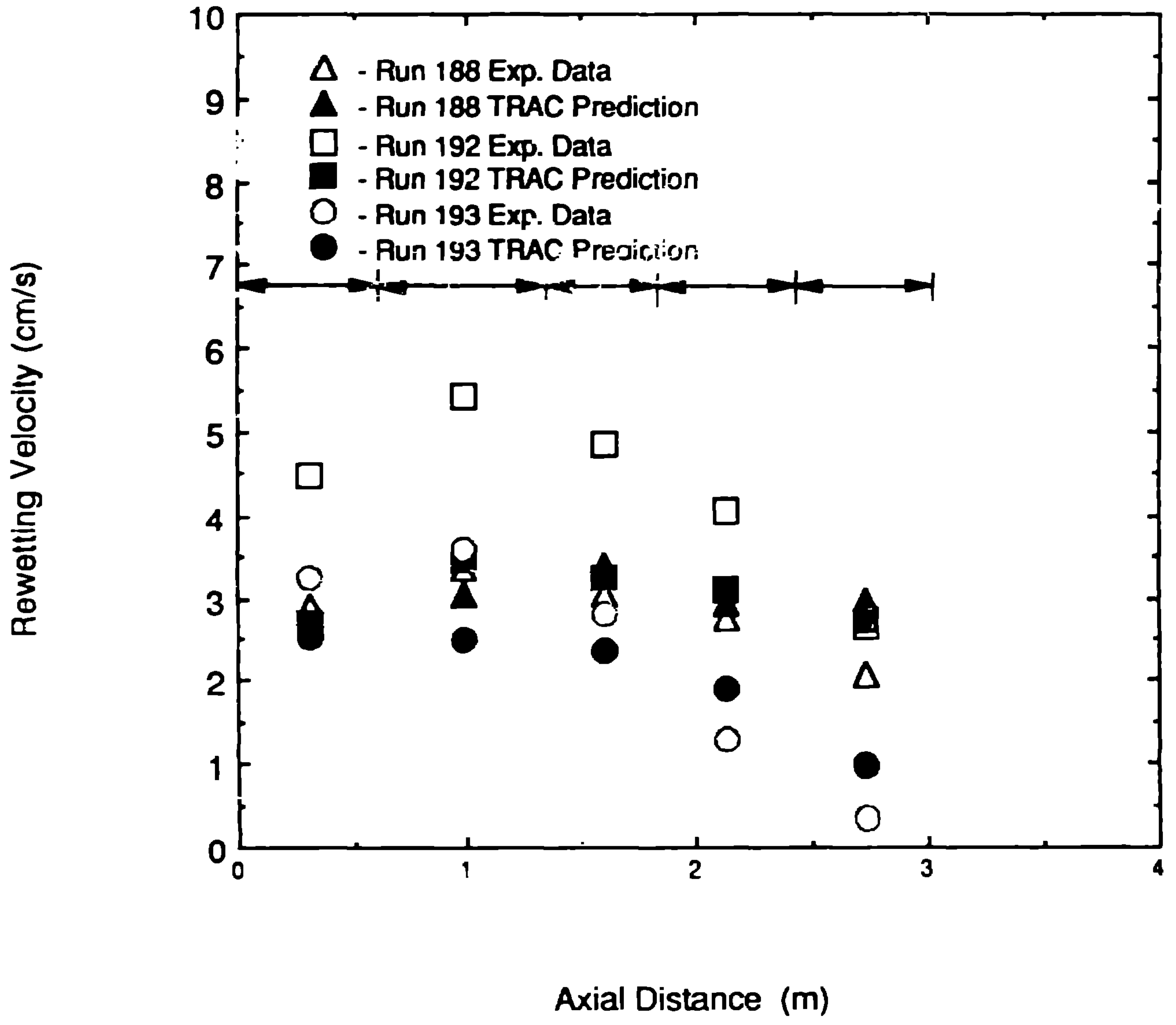

Fig. 22. The Predicted and Measured Average Rewetting Velocity Between Thermocouple Locations for Berkeley Runs 188, 192 and 193.

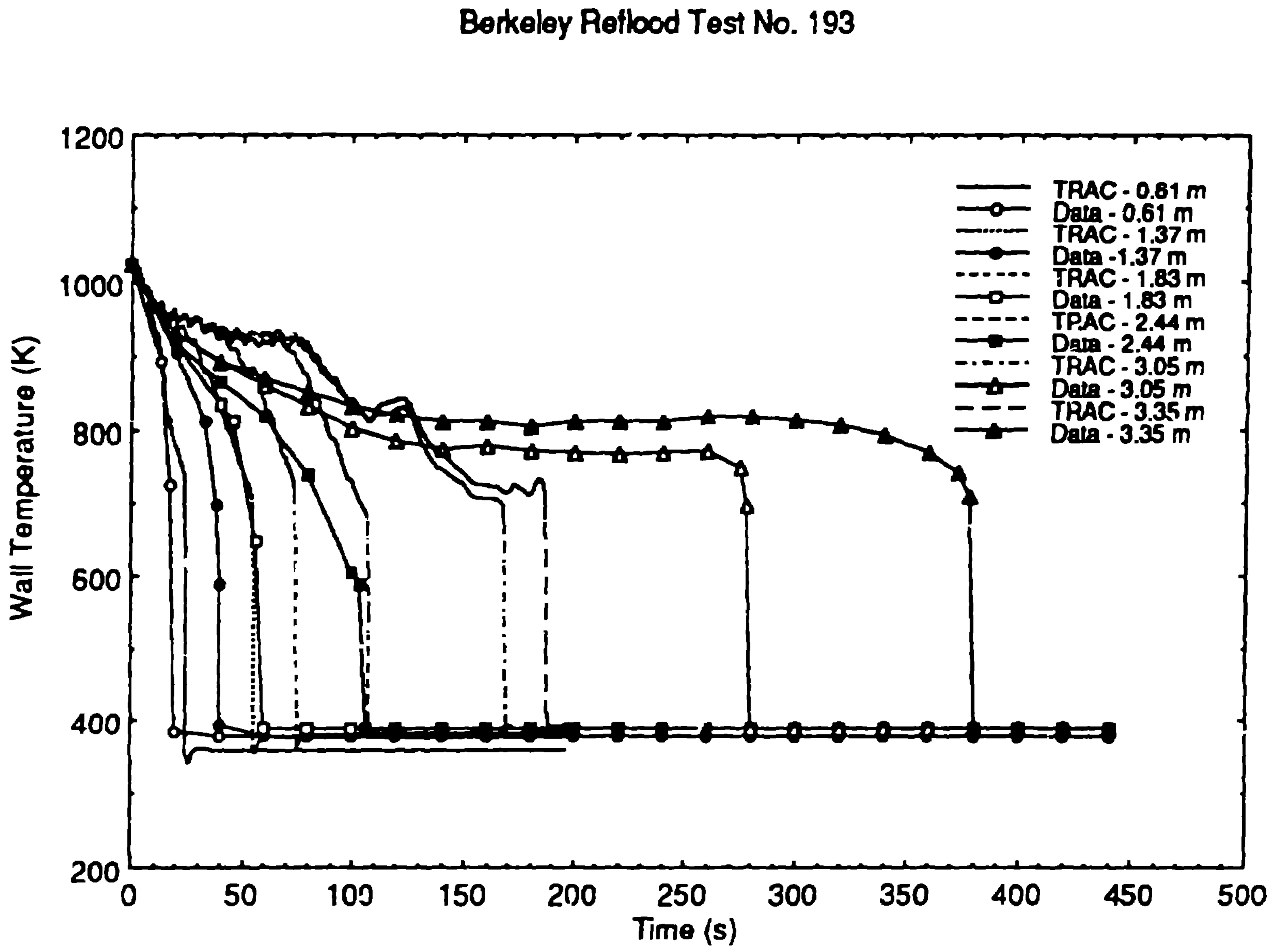

Fig. 23. The Predicted and Measured Wall Temperature Histories at Five Thermocouple Locations For Berkeley Run 193.

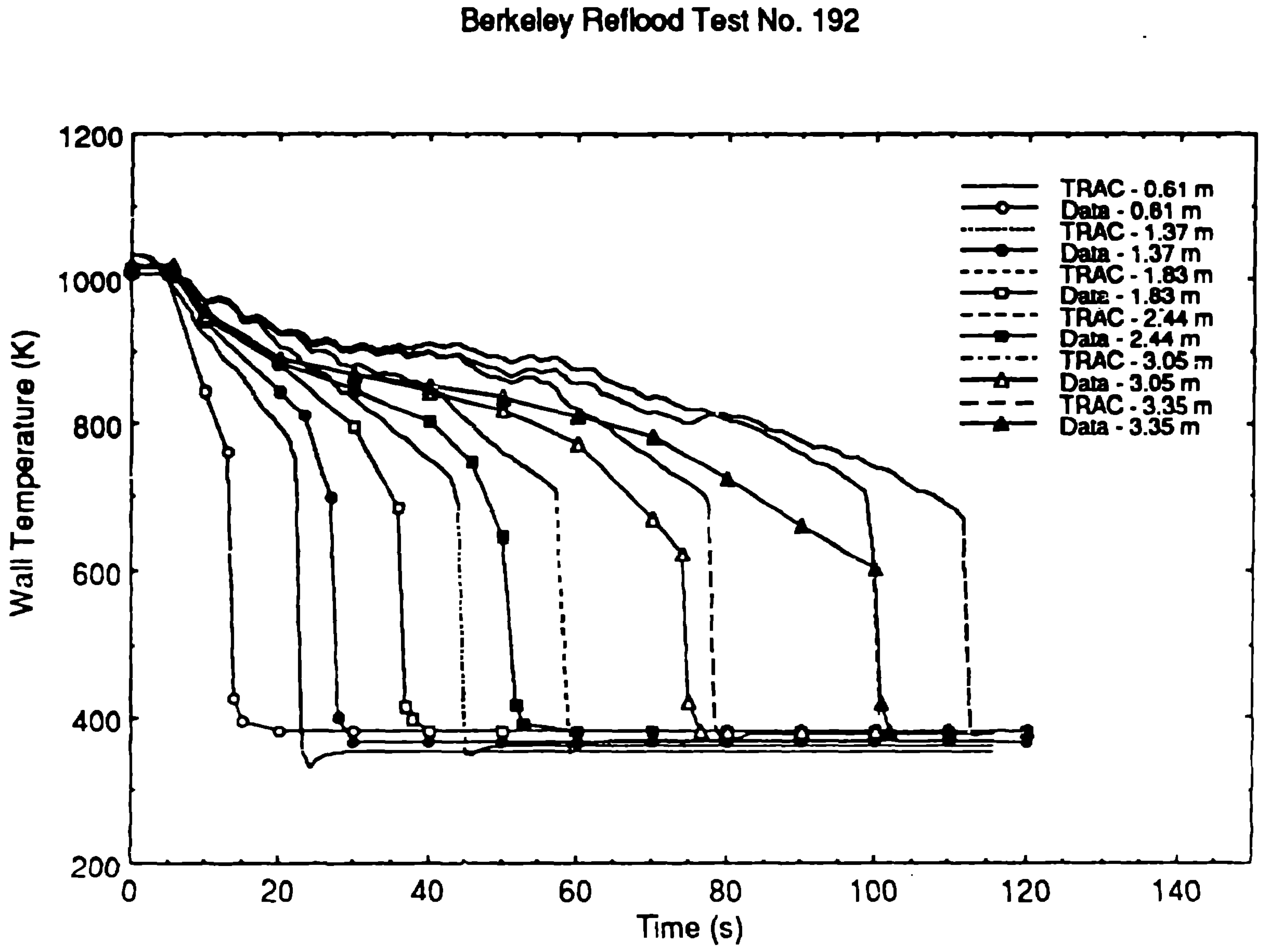

Fig. 24. The Predicted and Measured Wall Temperature Histories at Five Thermocouple Locations For Berkeley Run 192.

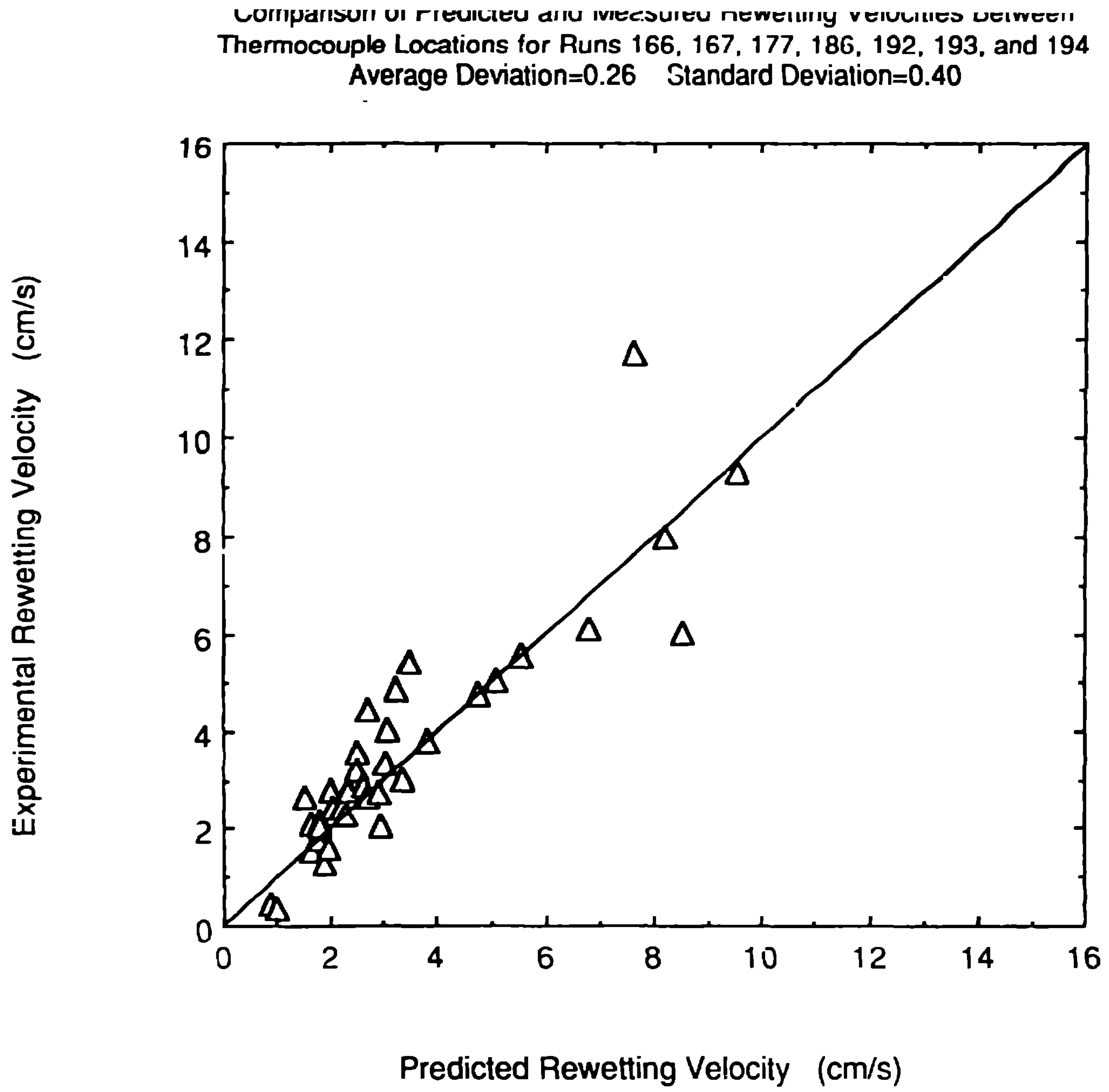

Fig. 25. The Predicted and Measured Average Rewetting Velocity Between Thermocouple Locations for all Berkeley Run considered in this work.